Available online at www.sciencedirect.com
ScienceDirect
Geochimica et Cosmochimica Acta 71 (2007) 165–185
Geochimica
www.elsevier.com/locate/gca

Determining accurate temperature–time paths from U–Pb thermochronology: An example from the Kaapvaal craton, southern Africa

Blair Schoene *, Samuel A. Bowring

Department of Earth, Atmospheric and Planetary Sciences, Room 54-1116, 77 Massachusetts Ave., Massachusetts Institute of Technology, Cambridge, MA 02139, USA

Received 14 April 2006; accepted in revised form 23 August 2006

Abstract

Thermochronology has revolutionized our understanding of the establishment and evolution of lithospheric thermal structure. However, many potential benefits provided by the application of diffusion theory to thermochronology have yet to be fully exploited. This study uses apatite ($T_c = 450$–550 °C) and titanite ($T_c = 550$–650 °C) U–Pb ID-TIMS thermochronology at the single- to sub-grain scale to separate the variable effects of volume diffusion of Pb from metamorphic (over)growth above and below the T_c of a mineral. Data are presented from two ca. 3227 Ma tonalite samples from north and south of the Barberton Greenstone Belt (BGB), southern Africa. Two distinct populations of apatite from a sample north of the BGB record fast cooling followed by metamorphic growth ~10 Myr later. Both apatite and titanite dates from south of the BGB show a strong correlation with the grain size and record 100 Myr of post-emplacement cooling. Complex core–rim zoning observed in cathodoluminescence images of apatite is interpreted to reflect metamorphic overgrowth above the T_c. The age and topology of grain size versus date curves from titanite and apatite are used in combination with a finite-difference numerical model to show that slow, non-linear, cooling and not thermal resetting is responsible for the observed distribution. The thermal histories from either side of the BGB are very different and provide unique insight into the BGB's tectonic evolution: a ~70 Myr period of apparent stability after ca. 3.2 Ga terrane assembly was followed by fast exhumation south of the BGB that led to lower-crustal melting and intrusion of granitic batholiths ca. 3.14–3.10 Ga.

1. Introduction

The integration of radiogenic isotope geo- and thermochronology with petrologic and tectonic studies is the only way to directly quantify lithospheric thermal structure as a function of time. Typically, a cooling date in a mineral is described by the closure temperature (T_c) concept of Dodson (1973, 1986). This model is based on the assumption that an isotopic date is the result of volume diffusion of the daughter product through the crystal lattice over time (t), and is therefore fundamentally a function of temperature (T). Interpreting mineral isotopic dates using Dodson's equation for T_c is subject to experimentally determining the physical diffusivity characteristics of an element in a crystal lattice (D_o and E), assuming that diffusion operates over a specified cooling rate (dT/dt) and within some idealized geometric shape with an effective diffusion dimension, a, ideally corresponding to the grain radius (see also reviews in Ganguly and Tirone, 1999; McDougall and Harrison, 1999; Hodges, 2003). Most studies use Dodson's theory as a qualitative construct and assume a nominal closure temperature for a given system, which proves to be valid on a semi-quantitative level, in that cooling dates are often consistent with well-understood geology and maintain relative consistency in ages among different thermochronometers. Empirical estimates of closure temperatures for a variety of U–Pb, $^{40}Ar/^{39}Ar$, (U–Th)/He, and Sm–Nd, and fission track thermochronometers from natural settings are broadly consistent with

* Corresponding author.
E-mail address: schoene@mit.edu (B. Schoene).

0016-7037/$ - see front matter © 2006 Elsevier Inc. All rights reserved.
doi:10.1016/j.gca.2006.08.029

predictions based on experimental determination of physical diffusion parameters (e.g. Harrison, 1981; Harrison et al., 1985; Cherniak et al., 1991; Cherniak, 1993; Ganguly et al., 1998; Cherniak and Watson, 2001; Ducea et al., 2003; Reiners and Ehlers, 2005) and theoretical estimates based on ionic porosity (Dahl, 1997). In reality, many of the assumptions that go into Dodson's formulation are likely to be compromised in real geologic scenarios, and the result is that distributions of cooling dates are often much more precise than our ability to interpret them. For example, application of Dodson's (1973, 1986) formulation becomes limited for large grain sizes with fast cooling (Ganguly and Tirone, 1999) and in conditions of nonmonotonic cooling or isothermal holding (Dodson, 1973), or in rocks where thermal resetting of dates is important (Dodson, 1975).

Furthermore, microanalytical $^{40}Ar/^{39}Ar$ studies have shown that the assumption of volume diffusion is not always valid, in that dates may be controlled by, for example, deformation-related microsctructure or solid-state recrystallization (Wartho, 1995; Dunlap and Kronenberg, 2001; Mulch et al., 2002). Comparable studies within the U–Pb system are relatively few, though it is well known that titanite can be involved in a host of metamorphic reactions from granulite to greenschist grade conditions (Spear, 1993; Frost et al., 2000; Lucassen and Becchio, 2003)—well below its T_c of 550–650 °C (Corfu, 1988; Cherniak, 1993; Hawkins and Bowring, 1999). Multiple generations of titanite in single rocks have been identified based on optical microscopy, back-scattered electron imaging, petrography, and both ID-TIMS and SIMS U–Pb geochronology (Franz and Spear, 1985; Gromet, 1991; Verts et al., 1996; Corfu and Stone, 1998; Aleinikoff et al., 2002). Apatite ($T_c \approx 450$–550 °C; Cherniak et al., 1991; Chamberlain and Bowring, 2000) is also stable in a wide range of metamorphic conditions (Bingen et al., 1996; Pan and Fleet, 1996; Bea and Montero, 1999), as well as in low-T fluid-rich environments (Smith and Yardley, 1999; Spear and Pyle, 2002). Metamorphic reequilibration below the T_c of thermochronometers jeopardizes closed-system behavior and therefore may lead to erroneous interpretations of mineral dates.

An independent constraint on whether volume diffusion is controlling a recorded date resides in that Dodson's (1973) theory predicts a distribution in closure dates as a function of grain size (here called the a–t curve). Though both metamorphic overgrowth and volume diffusion predict a younging in age towards the outside of a grain (Fig. 1), volume diffusion alone predicts a correlation with grain size. Wright et al. (1991) documented a relationship between $^{40}Ar/^{39}Ar$ closure dates in biotite and grain diameter and used manipulations of Dodson's equation to calculate dT/dt over its closure interval. Hawkins and Bowring (1999) use the a–t curve to calculate T–t curves for a suite of titanite grains from a slowly cooled Proterozoic terrane. Several U–Pb studies have documented crude a–t curves for rutile (Mezger et al., 1989; Schmitz and Bowring, 2003), suggesting its grain size may also act as the effective diffusion dimension.

Perhaps a more difficult problem arises from the fact that both slow cooling and thermal resetting in U–Pb, $^{40}Ar/^{39}Ar$ and other thermochronometers should result in robust a–t curves. Because of the assumption that T varies with $1/t$ in Dodson's (1973) formulation, quantitatively testing the effect of partial thermal resetting is not possible with that model (Dodson, 1973, 1975). Therefore, most studies approach the problem of resetting by qualitatively weighing the importance of previously documented local or regional geologic thermal anomalies (e.g. Layer et al., 1992; Pidgeon et al., 1996; Ketchum et al., 1998). Some studies have shown, however, that thermal modeling with reasonable geologic constraints is useful in testing the likelihood and the effect of resetting in the U–Pb system (Verts et al., 1996; Schmitz and Bowring, 2003), though none of these studies incorporate complicated, non-linear T–t paths.

In this study, we use U–Pb ID-TIMS thermochronology to investigate the competing processes controlling U–Pb closure dates in apatite and titanite. We utilize two ca. 3227 Ma tonalites with contrasting thermal histories from north and south of the Barberton greenstone belt (BGB), SE Kaapvaal craton, southern Africa. The minerals' growth histories are inferred from petrographic characterization and by back-scattered electron (BSE) and cathodoluminescence (CL) imaging. A combination of whole grain

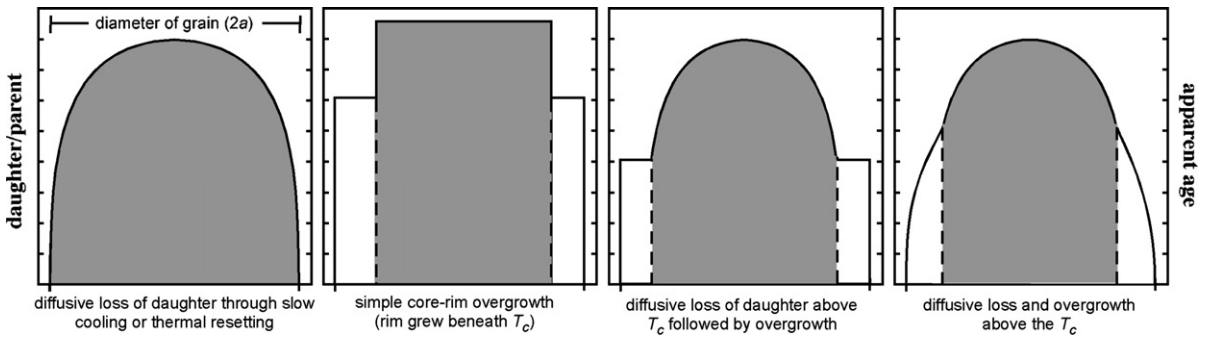

Fig. 1. 1-D depiction of age distributions within thermochronometers as a function of radius resulting from different thermal and metamorphic histories.

and microsampled apatite are used to document age gradients as a function of grain size and zoning characteristics. Air-abraded and unabraded single grains of titanite were also analyzed to investigate *a–t* relationships and intragrain date gradients. Finally, we use a finite-difference numerical model that calculates *a–t* curves for different thermal histories to test whether the observed *a–t* curves are a result of slow cooling or resetting. Though previously hypothesized (e.g. Watson and Harrison, 1984), we show for the first time that *a–t* curves from multiple thermochronometers with different nominal T_c can be used together to constrain unique thermal histories for rocks.

2. Mesoarchean evolution of the Kaapvaal craton

The southeast portion of the Kaapvaal craton is characterized by a protracted evolution during the Mesoarchean that culminated in a period of orogenesis and continental assembly ca. 3.2 Ga (Fig. 2). The study area has traditionally been divided into several terranes, including the Barberton Greenstone Belt (BGB; Anhaeusser, 1969; Viljoen and Viljoen, 1969; Lowe and Byerly, 1999) and the Ancient Gneiss Complex (AGC; Hunter et al., 1978; Jackson, 1984; Compston and Kröner, 1988). The AGC is composed primarily of banded felsic to mafic orthogneisses which intruded and were metamorphosed and deformed during several distinct periods at 3.55–3.50 Ga, ca. 3.45 Ga, and ca. 3.23 Ga (Hunter et al., 1978; Jackson, 1979, 1984; Kröner et al., 1989; Schoene and Bowring, 2004; Compston and Kröner, 1988). The BGB was erupted, intruded, and deposited over roughly the same period of time, but is composed of dominantly supracrustal rocks including mafic to ultramafic lavas, cherts, banded iron formations, and a heterogeneous sequence of siliciclastics (Anhaeusser, 1969; Viljoen and Viljoen, 1969; Condie et al., 1970; Anhaeusser, 1976; Eriksson, 1980; de Wit, 1982; de Wit et al., 1987; Lowe and Byerly, 1999). Also present along the margins of the BGB are plutonic rocks, ranging in composition from tonalitic to granitic, which give ages that fall roughly into four age groups: ca. 3.51, 3.45, 3.23 and 3.11 Ga (Anhaeusser et al., 1981; Armstrong et al., 1990; Kamo and Davis, 1994; Kisters and Anhaeusser, 1995; de Ronde and Kamo, 2000; Westraat et al., 2005).

An important aspect of the thermotectonic history of the region involves the juxtaposition of lower-grade rocks of the BGB and the higher-grade plutonic complexes that surround them. P–T estimates and $^{40}Ar/^{39}Ar$ hornblende data show that portions of the BGB were never subjected to metamorphic grades above greenschist to lower-amphibolite (Cloete, 1991; Lopez Martinez et al., 1992; Xie et al., 1997). To the south of the BGB, slivers of mafic semipelites within the plutonic complexes yield P–T estimates from upper-amphibolite to granulite grade conditions (Dziggel et al., 2002; Stevens et al., 2002; Kisters et al., 2003; Diener et al., 2005). A period of major convergent tectonism and inferred terrane accretion ca. 3.23 Ga imposed the dominant NE–SW structural trend of the belt (Jackson et al., 1987; de Ronde and de Wit, 1994; Heubeck and Lowe, 1994; Kamo and Davis, 1994; Lowe, 1999; de Ronde and Kamo, 2000), and may be responsible for the high-grade metamorphism in the plutonic complexes at the south of the belt (Dziggel et al., 2002; Stevens et al., 2002; Kisters et al., 2003; Diener et al., 2005). Following NW–SE convergent tectonism, there was a transition towards NE–SW strike-slip to transtensional faulting through at least the central belt (Jackson et al., 1987; de Ronde and de Wit, 1994; de Ronde and Kamo, 2000). Extensional kinematics are inferred to be either the result of a gravitational collapse immediately following ca. 3.23 Ga orogenesis (Kisters et al., 2003) or ~100 Myr later contemporaneous with ca. 3.11 Ga granitic intrusions (Jackson et al., 1987; de Ronde and de Wit, 1994; Kamo and Davis, 1994; Westraat et al.,

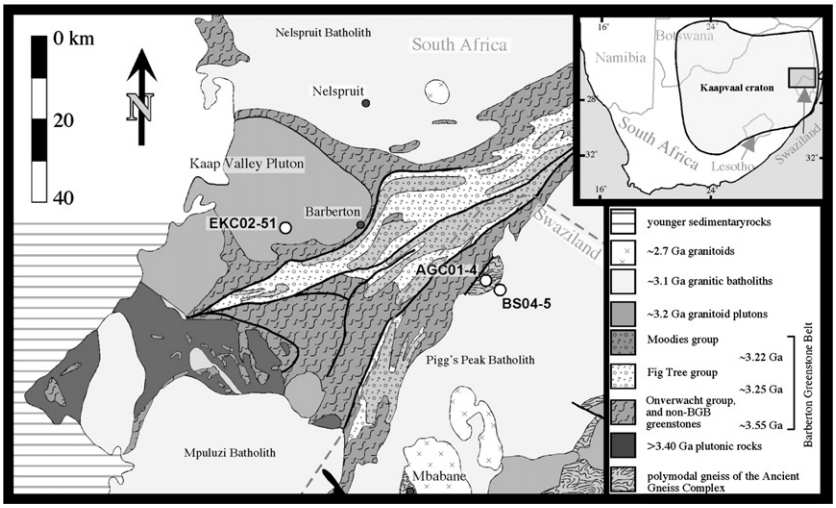

Fig. 2. Location map of the eastern Kaapvaal craton. Sample locations are shown; see text for discussion. Outlined box in inset shows enlarged area. Geology compiled from Kröner et al. (1989), Lowe and Byerly (1999), and Wilson (1982). Age information from Armstrong et al. (1990), Byerly et al. (1996), de Ronde and Kamo (2000), de Ronde et al. (1991), Kamo and Davis (1994), Kröner et al. (1989), Kröner et al. (1996), and Schoene and Bowring (2004).

2005). Our objective in this study is to use U–Pb thermochronology on apatite and titanite to calculate thermal histories of rocks both N and S of the BGB that can then be used in concert with structural studies and existing thermochronology to construct robust thermotectonic models that help explain the differential exhumation of rocks evidenced in the surface geology.

3. Analytical methods

3.1. Electron microprobe analysis

The MIT JEOL 733 Superprobe electron microprobe (EMP) facility was used for making cathodoluminescence (CL) and backscatter-electron (BSE) images of zircon, titanite and apatite. Minerals were hand-picked based on varying morphology, color, and clarity, were mounted in epoxy resin, and were polished, cleaned, and carbon-coated. BSE and CL images were collected using a 15 keV accelerating voltage and the beam current was varied between 4 and 80 nA depending on the intensity of the luminescence.

3.2. U–Pb analytical procedure

Minerals were extracted from rock samples by standard crushing, Wilfley table, heavy-liquid and magnetic separation. Zircon fractions were pre-treated with either the air-abrasion (Krogh, 1982) or chemical-abrasion (Mattinson, 2003, 2005) technique. Air-abraded zircons and both air-abraded and unabraded titanite fractions were ultrasonicated in 30% HNO_3 for an hour, fluxed in 30% HNO_3 at ~80 °C for an hour, and rinsed in ultrapure acetone and H_2O before being loaded into 300 μl Teflon FEP microcapsules and spiked with a mixed ^{233}U–^{235}U–^{205}Pb tracer. Zircon and titanite were dissolved in Parr bombs in ~120 μl of 29 M HF with ~25 μl of 30% HNO_3 at ~210 °C for 48 h, dried and re-dissolved in 6 M HCl at ~180 °C overnight. For the chemical-abrasion technique, zircons were placed in a muffle furnace at 900 ± 20 °C for ~60 h in quartz beakers before being transferred to 300 μl Teflon FEP microcapsules and leached in ~120 μl of 29 M HF + ~25 μl of 30% HNO_3 for 12–14 h at ~180 °C. The acid was removed from the capsules and the fractions were then rinsed in ultrapure H_2O, fluxed on a hotplate at ~80 °C for an hour in 6 M HCl, and rinsed in ultrapure H_2O and 30% HNO_3. Fractions were then spiked and fully dissolved using the procedure described above.

Imaged apatite grains were broken and removed from epoxy resin by pushing a stainless steel tool into the epoxy next to the desired grain. All apatite fractions were handpicked, rinsed and ultrasonicated in ultrapure H_2O and acetone prior to loading into single 300 μl FEP teflon microcapsules. Apatite was then spiked with the mixed ^{233}U–^{235}U–^{205}Pb tracer and dissolved in 12 N HCl overnight in a Parr bomb at 180 °C, dried down and redissolved in 6 N HCl overnight.

Clear, non-metamict, and inclusion-free feldspar grains, handpicked from non-magnetic separates, were ultrasonicated in ultrapure H_2O. Step-wise leaching of feldspar followed the procedure of Housh and Bowring (1991), modified to account for smaller sample size.

U and Pb were separated using an HCl-based single-column (zircon) or an HBr-based two-column (titanite, apatite, and feldspar leachates) anion exchange chemistry modified after Krogh (1973). Isotopic measurements were performed on a VG Sector-54 multi-collector thermal-ionization mass spectrometer at MIT. Pb and U were either loaded together (HCl-based chemistry) or on separate (HBr-based chemistry) Re filaments in a silica-gel/phosphoric acid mixture (Gerstenberger and Haase, 1997). Pb was measured by either (1) peak-hopping on a single Daly detector (for smaller beams), (2) a dynamic Faraday–Daly routine (F–D), or (3) for feldspar analyses with large 204 peaks, in static Faraday mode. U isotopic measurements were made in static Faraday mode. Mass fractionation on the Daly detector was determined to be 0.25 ± 0.04%/a.m.u. over a wide temperature range based on analysis of the NBS-981 common Pb standard and spiked aliquots of NBS-983. Mass fractionation and detector bias on the F–D and static Faraday routines was determined to be 0.07 ± 0.04%/a.m.u. U mass fractionation is monitored using a double spike. All common Pb for the zircon analyses was attributed to procedural blank. Total procedural Pb blanks for the HBr-based chemistry (apatite and titanite) were determined to be 1.5 ± 0.4 pg. K-feldspar leachates were assigned a Pb blank of 10 pg based on the amount of reagent used in the procedure, though the blank is a negligible proportion of the total Pb in those analyses. U blanks are assigned a value of 0.10 ± 0.05 pg. All samples were spiked with a ^{205}Pb–^{233}U–^{235}U tracer, whose calibration is detailed in Schoene et al. (2006), in which an error of ±0.015% is assigned to the $^{205}Pb/^{235}U$ of the tracer. U–Pb data reduction was performed using the algorithms of Ludwig (1980).

4. Sample descriptions and U–Pb results

4.1. EKC02-51 (Kaap Valley pluton)

EKC02-51 comes from the Kaap Valley pluton, a multiphase intrusion located north of the Barberton Greenstone Belt (Fig. 2). Several previous geochronologic studies have reported U–Pb and $^{40}Ar/^{39}Ar$ dates for the pluton (Armstrong et al., 1990; Layer et al., 1992; Kamo and Davis, 1994; Schoene et al., 2006). Kamo and Davis (1994) and Schoene et al. (2006) report identical $^{207}Pb/^{206}Pb$ dates of 3227 ± 1 and 3227.2 ± 0.2 Ma, respectively, which are interpreted to be the time of igneous crystallization (this study uses the same sample as in Schoene et al., 2006). The date from Kamo and Davis (1994) included both zircon and titanite fractions, indicating fast post-crystallization cooling through ~600 °C. $^{40}Ar/^{39}Ar$ hornblende dates of ca. 3212 Ma

also support fast post-intrusion cooling (Layer et al., 1992).

Our sample of the Kaap Valley pluton was collected from a fresh roadcut several kilometers east of the pass on R61 between Badplaas and Barberton. EKC02-51 is a weakly foliated fine-grained biotite tonalite containing abundant pristine zircon and apatite, but no titanite or hornblende. Thin-section analysis reveals significant low-grade metamorphism in this rock, including chloritization of biotite and secondary epidote, clinozoisite and sericite. Mineral separates reveal two end-member populations of apatite that differ according to magnetic susceptibility, habit, and color. One end-member group is non-magnetic, clear, and of variable habit. The second end-member is primarily found in the more magnetic separates, is light blue and translucent, and form both stubby euhedral hexagonal prisms and subhedral grains. BSE images of both populations reveal no internal zonation, while CL images show patchy zoning of unclear origin (Fig. 3). There is a gradient between the two end-member populations, and so a range of grains was chosen for analysis. The different populations are difficult to distinguish in thin-section, though large (>250 μm in diameter) and/or euhedral grains are only found along grain boundaries and/or associated with biotite. Subhedral cylinders and barrels are found as inclusions in plagioclase and quartz.

Apatite from this sample was analyzed for U–Pb systematics (Table 1), including seven whole single-grains, two multi-grain fractions (a1 and a2 each had two grains), and four grains that were removed from grain mount. Three grains from grain mount were broken in half prior to analysis. The $^{207}Pb/^{206}Pb$ dates form two distinct populations (Figs. 3 and 4). Fig. 5 shows the $^{207}Pb/^{206}Pb$ dates as a function of grain size. The older, ca. 3225–3220 Ma population shows a slight trend towards younger $^{207}Pb/^{206}Pb$ dates with smaller grain size, such that the MSWD of equivalence is 8.0 (Ludwig, 1998), though it is unclear whether this trend reflects cooling. The younger population gives a weighted mean $^{207}Pb/^{206}Pb$ date of 3213.0 ± 0.5 Ma (MSWD = 0.8; excluding one negatively discordant analysis, a1.29a). Of the two grains that were successfully halved and analyzed, two shards from one grain gave identical results, while one of the shards from the other broken grain (a1.29a) was negatively discordant and yielded a much younger $^{207}Pb/^{206}Pb$ date. One other grain (a1.30) was −0.7% discordant, but gave an identical $^{207}Pb/^{206}Pb$ date to the younger population. All of the other analyses plot between ~0.0% and ~0.3% discordant and have radiogenic Pb to common Pb (Pb^*/Pb_c) ratios between ~3 and ~14 (Table 1).

4.2. AGC01-4

This sample is a biotite tonalite from an inlier of highly deformed plutonic basement rocks adjacent to the southeast margin of the BGB (Fig. 2). From near this locality, Compston and Kröner (1988) and Kröner et al. (1989) reported ion-microprobe U–Pb dates of zircon from multiple samples that show a complex and enigmatic growth history between ca. 3.6 and 3.1 Ga. Our sample comes from an outcrop on the Phophonyane river, approximately 1 km north of the main highway, from a unit that clearly cross-cuts the oldest phases of bimodal gneiss in the area, but is foliated parallel to the local fabric in those rocks. This sample yielded abundant zircon, titanite and apatite, which were analyzed for U–Pb systematics.

4.2.1. Zircon

Zircon grains from this sample are stubby to elongate dully-faceted prisms ranging in length from ~30 to 200 μm. The least magnetic separate yielded abundant cloudy to translucent grains, which reveal oscillatory zoning in BSE images, typical of magmatic zircons (see Corfu et al., 2003; Fig. 6). Fifteen air-abraded grains and nine chemical-abraded grains were analyzed for U–Pb isotope systematics. Three chemical-abraded grains are within error of concordia and these analyses give a weighted mean $^{207}Pb/^{206}Pb$ date of 3226.1 ± 0.7 Ma (MSWD = 0.2; Fig. 7).

4.2.2. Titanite

Titanite is light to dark brown in color and ranges in size from <50 to 250 μm (diameters measured as the average of the three principle axes) and is subhedral to anhedral in mineral separates. BSE images of titanite grains show faint oscillatory zoning in subhedral fragments (Fig. 6). Thin-section analysis reveals that titanite is primarily euhedral and can be as large as 500 μm, suggesting that many grains were broken during the crushing process. For this reason, only the most euhedral grains were selected, though this is an imperfect process. Eleven single grain fractions and two fractions consisting of two grains each (s4 and s7) were

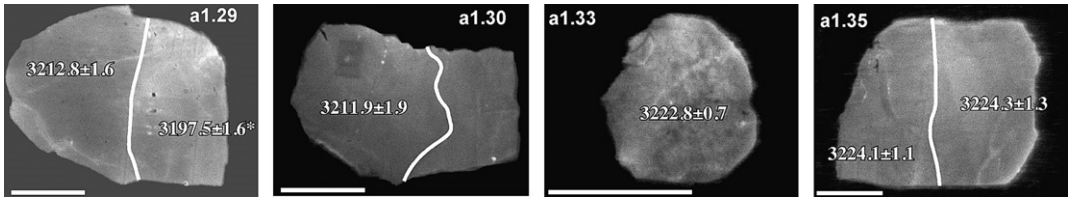

Fig. 3. Cathodoluminescence images of apatite from EKC02-51 (Kaap valley pluton), with fraction number in top corner. White lines are where grains were broken prior to removal from grain mount, and the corresponding $^{207}Pb/^{206}Pb$ dates are shown (*this analysis is very negatively discordant). U–Pb data are in Table 1. Scale bars are 100 μm. Errors are at the 95% confidence interval.

Table 1
U–Pb isotopic data

Sample[a]	# grains	Grain diameter[b]	Pb*/Pb$_c$[c]	Pb$_c$ (pg)[d]	Th/U[e]	Isotopic ratios									Dates (Ma)			% disc.[j]
						$^{206}Pb/^{204}Pb$[f]	$^{208}Pb/^{206}Pb$[g]	$^{206}Pb/^{238}U$[g]	% err[h]	$^{207}Pb/^{235}U$[g]	% err[h]	$^{207}Pb/^{206}Pb$[g]	% err[h]	corr. coef.	$^{206}Pb/^{238}U$[i]	$^{207}Pb/^{235}U$[i]	$^{207}Pb/^{206}Pb$[i]	
EKC02-51 (Kaap Valley pluton)																		
Apatite																		
a1	2	90	3.8	14.5	0.04	198	0.011	0.645753	0.16	22.67103	0.22	0.25463	0.12	0.839	3211.6	3212.9	3213.8	0.09
a2	2	110	3.2	32.3	0.04	165	0.010	0.648107	0.17	22.90351	0.19	0.25630	0.08	0.904	3220.8	3222.9	3224.1	0.13
a4	1	170	5.1	29.7	0.09	254	0.023	0.646260	0.15	22.68531	0.17	0.25459	0.08	0.893	3213.6	3213.5	3213.5	0.00
a5	1	240	5.4	43.2	0.03	273	0.007	0.644832	0.09	22.62546	0.11	0.25448	0.06	0.827	3208.0	3211.0	3212.8	0.19
a6	1	110	5.2	14.9	0.02	268	0.006	0.648154	0.11	22.89598	0.13	0.25620	0.06	0.880	3221.0	3222.5	3223.5	0.10
a7	1	100	13.9	22.9	0.07	677	0.020	0.647802	0.08	22.87322	0.09	0.25608	0.05	0.852	3219.6	3221.6	3222.8	0.12
a8	1	200	7.8	66.2	0.03	386	0.009	0.647884	0.05	22.91164	0.07	0.25648	0.05	0.744	3219.9	3223.2	3225.2	0.21
a9	1	225	6.6	71.0	0.00	337	0.001	0.648811	0.08	22.94491	0.10	0.25649	0.05	0.856	3223.6	3224.6	3225.3	0.07
a10	1	275	8.7	113.3	0.03	427	0.007	0.646082	0.07	22.78394	0.08	0.25576	0.05	0.814	3212.9	3217.8	3220.8	0.31
a1.29a	<1	250	5.1	5.8	0.03	268	0.009	0.654559	0.23	22.74551	0.26	0.25203	0.10	0.918	3246.0	3216.1	3197.5	−1.93
a1.29b	<1	250	9.4	13.9	0.01	473	0.004	0.645059	0.09	22.63267	0.11	0.25447	0.06	0.856	3208.9	3211.3	3212.8	0.15
a1.30a	<1	120	3.1	10.0	0.02	164	0.005	0.650454	0.34	22.80895	0.36	0.25432	0.12	0.944	3230.0	3218.8	3211.9	−0.72
a1.33	<1	90	6.8	22.6	0.02	341	0.005	0.646313	0.06	22.80567	0.08	0.25592	0.05	0.741	3213.8	3218.7	3221.7	0.31
a1.35a	<1	150	7.5	22.7	0.01	374	0.003	0.647730	0.07	22.89238	0.11	0.25633	0.09	0.625	3219.3	3222.4	3224.3	0.20
a1.35b	<1	150	7.3	21.9	0.01	366	0.003	0.646910	0.09	22.86110	0.11	0.25630	0.07	0.790	3216.1	3221.0	3224.1	0.31
AGC01-4																		
Zircon																		
z1	1	—	47.9	2.6	0.22	2453	0.071	0.528134	0.23	18.06069	0.29	0.24802	0.17	0.816	2733.6	2993.0	3172.2	16.92
z2	1	—	180.5	1.4	0.18	10143	0.068	0.437855	0.12	14.41993	0.14	0.23885	0.06	0.905	2341.0	2777.7	3112.4	29.45
z4	1	—	79.4	4.2	0.23	3885	0.073	0.523614	0.16	17.68981	0.17	0.24502	0.08	0.900	2714.5	2973.0	3152.9	17.00
z5	1	—	13.6	11.3	0.22	645	0.079	0.482140	0.14	16.03199	0.16	0.24116	0.06	0.918	2536.6	2878.7	3127.7	22.79
z6	1	—	19.3	5.0	0.17	953	0.054	0.537140	0.15	18.29210	0.17	0.24699	0.06	0.929	2771.5	3005.2	3165.6	15.28
z7	1	—	4.7	20.8	0.24	231	0.079	0.523837	0.21	17.74783	0.23	0.24572	0.08	0.931	2715.4	2976.2	3157.4	17.11
z9	1	—	1.6	12.8	0.44	81	0.174	0.411169	0.73	12.91834	0.76	0.22787	0.15	0.981	2220.3	2673.7	3037.1	31.68
z10	1	—	2.7	12.2	0.44	133	0.120	0.632324	0.39	22.25520	0.42	0.25526	0.15	0.935	3158.8	3194.9	3217.7	2.32
z11	1	—	7.2	11.3	0.26	349	0.094	0.452246	0.25	14.22166	0.30	0.22807	0.16	0.851	2405.2	2764.6	3038.6	24.90
z12	1	—	2.2	4.7	0.33	118	0.091	0.636983	0.79	22.51567	0.81	0.25636	0.15	0.982	3177.1	3206.2	3224.5	1.86
z13	1	—	21.0	3.2	0.39	980	0.147	0.442169	0.23	14.49386	0.24	0.23774	0.07	0.953	2360.3	2782.6	3104.9	28.54
z14	1	—	14.5	1.1	0.03	847	0.014	0.334743	0.54	11.35342	0.55	0.24599	0.07	0.992	1861.3	2552.6	3159.1	47.07
z15	1	—	8.3	7.7	0.31	393	0.093	0.577756	0.16	19.68108	0.20	0.24706	0.11	0.837	2939.6	3075.8	3166.0	8.89
z18	1	—	0.5	25.1	0.85	30	0.357	0.389799	0.99	12.34292	1.11	0.22965	0.41	0.929	2121.9	2630.8	3049.6	35.56
z19	1	—	1.2	5.9	0.48	68	0.160	0.503230	1.11	16.42092	1.23	0.23666	0.44	0.935	2627.7	2901.6	3097.7	18.43
za1	1	—	18.0	8.8	0.20	845	0.059	0.590673	0.10	21.67507	0.11	0.26614	0.05	0.892	2992.2	3169.3	3283.4	11.07
za2	1	—	15.7	2.2	0.23	795	0.063	0.649166	0.32	22.97418	0.32	0.25667	0.05	0.986	3224.9	3225.8	3226.4	0.06
za5	1	—	36.0	1.1	0.12	2013	0.040	0.519119	0.25	18.24451	0.26	0.25490	0.06	0.973	2695.4	3002.7	3215.4	19.73
za6	1	—	82.2	0.6	0.21	4594	0.060	0.602185	0.07	21.16657	0.09	0.25493	0.05	0.827	3038.6	3146.3	3215.6	6.90
za7	1	—	61.0	0.7	0.21	3415	0.059	0.615876	0.11	21.64515	0.12	0.25490	0.06	0.887	3093.5	3167.9	3215.4	4.77
za10	1	—	32.9	1.9	0.18	1866	0.050	0.639734	0.13	22.65198	0.14	0.25681	0.05	0.926	3188.0	3212.1	3227.2	1.54
za12	1	—	9.7	0.3	0.13	565	0.035	0.646799	0.55	22.88202	0.60	0.25658	0.21	0.939	3215.7	3221.9	3225.8	0.40
za13	1	—	19.7	0.2	0.20	1119	0.053	0.648283	0.27	22.93540	0.29	0.25659	0.09	0.953	3221.5	3224.2	3225.9	0.17
za17	1	—	8.9	0.6	0.16	520	0.042	0.638487	0.46	22.57750	0.50	0.25646	0.17	0.940	3183.1	3208.9	3225.1	1.65
Titanite																		
s1	1	185	13.1	27.8	0.52	582	0.141	0.632054	0.12	21.58132	0.13	0.24764	0.06	0.896	3157.7	3165.1	3169.8	0.48
s2	1	180	6.9	120.0	0.23	332	0.063	0.629620	0.07	21.31665	0.11	0.24555	0.09	0.642	3148.1	3153.1	3156.3	0.33

s4	2	120	26.2	18.6	0.16	1247	0.044	0.632319	0.08	21.56202	0.10	0.24732	0.05	0.876	3158.8	3164.2	3167.7	0.36
s5	1	220	6.0	82.4	0.40	278	0.107	0.636272	0.13	21.90596	0.16	0.24970	0.08	0.876	3174.3	3179.6	3182.9	0.34
s6	1	210	14.8	41.8	0.36	680	0.096	0.633222	0.09	21.63886	0.10	0.24784	0.05	0.887	3162.3	3167.7	3171.0	0.35
s7	2	140	2.1	207.7	0.72	100	0.183	0.672447	0.11	23.00599	0.14	0.24813	0.08	0.809	3315.3	3227.2	3172.9	−5.75
s8	1	120	3.3	7.2	0.19	171	0.051	0.626553	0.15	20.96218	0.18	0.24265	0.08	0.889	3135.9	3136.8	3137.4	0.06
s9	1	130	4.5	7.0	0.14	233	0.038	0.627574	0.23	21.03517	0.26	0.24310	0.10	0.914	3140.0	3140.2	3140.4	0.02
s10	1	200	26.5	6.5	0.17	1285	0.045	0.630283	0.11	21.36701	0.12	0.24587	0.05	0.910	3150.7	3155.4	3158.4	0.31
s11	1	170	7.0	12.4	0.25	337	0.068	0.628332	0.14	21.22956	0.21	0.24505	0.13	0.789	3143.0	3149.1	3153.0	0.40
s12	1	190	4.7	21.6	0.31	227	0.083	0.631037	0.10	21.33124	0.12	0.24517	0.07	0.825	3153.7	3153.8	3153.8	0.01
s13	1	220	22.4	21.1	0.34	1027	0.091	0.633599	0.13	21.61638	0.14	0.24744	0.05	0.941	3163.8	3166.6	3168.4	0.19
s14	1	220	3.9	27.9	0.20	193	0.054	0.627092	0.22	21.03899	0.23	0.24333	0.08	0.939	3138.1	3140.4	3141.9	0.15
AGC01-4																		
Apatite																		
a1	5	70	4.1	24.2	0.29	207	0.078	0.619091	0.19	20.37702	0.25	0.23872	0.16	0.782	3106.3	3109.4	3111.4	0.21
a2	5	55	4.3	30.1	0.26	218	0.071	0.616424	0.19	20.20308	0.21	0.23770	0.08	0.919	3095.7	3101.1	3104.7	0.36
a3	1	170	3.6	62.0	0.18	184	0.050	0.621628	0.16	20.62574	0.18	0.24065	0.08	0.892	3116.4	3121.2	3124.2	0.32
a5	1	90	3.4	71.3	0.26	170	0.070	0.616814	0.11	20.23397	0.15	0.23792	0.09	0.802	3097.2	3102.6	3106.1	0.36
a6	1	235	3.0	66.6	0.29	152	0.078	0.623436	0.10	20.75546	0.14	0.24146	0.09	0.783	3123.6	3127.2	3129.6	0.24
a7	3	60	4.3	20.2	0.23	217	0.062	0.618845	0.20	20.31393	0.22	0.23807	0.10	0.889	3105.3	3106.4	3107.1	0.07
a8	1	40	1.4	3.7	0.35	88	0.095	0.613951	0.78	19.92355	0.87	0.23536	0.38	0.897	3085.8	3087.7	3088.9	0.12
a10	1	35	3.2	7.3	0.27	181	0.074	0.608771	0.29	19.52679	0.33	0.23264	0.16	0.877	3065.1	3068.2	3070.3	0.21
a11	1	90	3.9	9.6	0.29	202	0.077	0.623017	0.11	20.69392	0.19	0.24090	0.14	0.695	3121.9	3124.4	3125.9	0.16
a12	1	120	2.6	36.6	0.21	144	0.056	0.624977	0.25	20.86188	0.28	0.24210	0.12	0.895	3129.7	3132.2	3133.8	0.17
a13	1	180	2.3	45.6	0.21	123	0.056	0.629058	0.14	20.89147	0.21	0.24087	0.14	0.747	3145.9	3133.6	3125.7	−0.81
a14	1	240	3.1	109.4	0.27	159	0.073	0.624029	0.06	20.78611	0.09	0.24158	0.06	0.688	3125.9	3128.7	3130.4	0.18
a1.2a	<1	200	2.6	7.7	0.21	146	0.058	0.623147	0.49	20.73630	0.52	0.24135	0.16	0.951	3122.4	3126.3	3128.9	2.26
a1.2b	<1	200	2.5	6.3	0.19	151	0.050	0.625954	0.97	20.92664	0.99	0.24247	0.23	0.973	3133.6	3135.2	3136.3	0.11
a1.2c	<1	200	3.2	4.5	0.23	180	0.063	0.624124	0.62	20.79129	0.64	0.24161	0.16	0.969	3126.3	3128.9	3130.6	0.17
a1.2d	<1	200	3.6	11.8	0.25	189	0.067	0.622832	0.22	20.66060	0.25	0.24059	0.11	0.897	3121.2	3122.8	3123.8	0.11
a1.5a	<1	115	2.0	29.2	0.30	109	0.082	0.622059	0.18	20.61508	0.23	0.24035	0.14	0.815	3118.1	3120.7	3122.3	0.17
a1.5b	<1	115	2.5	21.8	0.29	134	0.079	0.618046	0.11	20.25586	0.16	0.23770	0.10	0.747	3102.1	3103.7	3104.6	0.10
a1.8	<1	250	3.2	63.1	0.19	165	0.053	0.627909	0.08	21.17324	0.10	0.24456	0.07	0.774	3141.3	3146.6	3149.9	0.34
a1.11	<1	200	2.4	30.1	0.28	127	0.076	0.618502	0.13	20.32761	0.27	0.23837	0.20	0.702	3104.0	3107.1	3109.1	0.21
a1.12	<1	180	2.0	40.5	0.30	109	0.081	0.616764	0.21	20.15648	0.23	0.23703	0.10	0.906	3097.0	3098.9	3100.1	0.13
a2.2	<1	120	2.4	19.5	0.32	125	0.087	0.621540	0.18	20.58156	0.23	0.24016	0.13	0.829	3116.0	3119.1	3121.1	0.20
a2.5a	<1	122	2.3	13.0	0.19	126	0.053	0.622345	0.14	20.64705	0.18	0.24062	0.11	0.789	3119.2	3122.2	3124.1	0.19
a2.5b	<1	122	1.3	4.7	0.36	79	0.098	0.618700	1.41	20.34661	1.43	0.23851	0.36	0.967	3104.7	3108.0	3110.1	0.22
a2.6	<1	65	3.3	11.2	0.30	170	0.082	0.616637	0.17	20.14140	0.21	0.23690	0.10	0.864	3096.5	3098.2	3099.2	0.11
a2.10	<1	130	1.2	14.7	0.40	73	0.105	0.643566	0.90	21.25535	0.92	0.23954	0.25	0.963	3203.0	3150.3	3116.9	−3.51
a2.14a	<1	50	1.6	6.7	0.48	92	0.129	0.606740	0.72	19.36093	0.78	0.23143	0.29	0.928	3056.9	3060.0	3062.0	0.21
a2.14b	<1	50	1.3	6.1	0.57	79	0.154	0.605331	1.27	19.28529	1.31	0.23106	0.36	0.962	3051.3	3056.2	3059.4	0.33
BSO4-5 (Pigg's Peak batholith)																		
Zircon																		
za1	1	—	520	0.23	0.49	20711	0.134	0.626060	0.11	21.00242	0.12	0.24331	0.05	0.918	3134.0	3138.7	3141.7	0.31
za2	1	—	1620	0.22	0.41	66197	0.110	0.625793	0.07	20.97847	0.08	0.24313	0.04	0.834	3132.9	3137.6	3140.6	0.31
za3	1	—	849	0.20	0.46	33785	0.124	0.624259	0.11	20.92089	0.12	0.24306	0.04	0.925	3126.8	3134.9	3140.1	0.53
za4	1	—	10907	0.16	0.41	405376	0.110	0.625586	0.05	20.96650	0.06	0.24307	0.04	0.772	3132.1	3137.0	3140.2	0.33
za5	1	—	15791	0.20	0.49	573023	0.134	0.624828	0.12	20.94386	0.12	0.24311	0.04	0.945	3129.1	3136.0	3140.4	0.45

(*continued on next page*)

Table 1 (*continued*)

[a] z1, z2, etc. are air-abraded zircons, za1, za2, etc. are chemical-abraded zircons.a1, a2, etc. are whole single grains or multiple grains; a1.xx, a2.xx are grains or grain fragments that were removed from grain-mount. s1, s2, etc. are whole grains or abraded grains.
[b] Numbers are in μm. Apatite diameter is that of a cylinder. Titanite diameter is average of 3 axes. Multi-grain fraction diameter is average of all grains.
[c] Ratio of radiogenic Pb (including 208Pb) to common Pb.
[d] Total weight of common Pb.
[e] Model Th/U ratio calculated from radiogenic 208Pb/206Pb ratio and 207Pb/206Pb age.
[f] Measured ratio corrected for spike and fractionation only. Mass fractionation corrections were based on analysis of NBS-981 and NBS-983. Corrections of 0.25 ± 0.04%/a.m.u. (atomic mass unit) and 0.07 ± 0.04%/a.m.u. were applied to single-collector Daly analyses and dynamic Faraday–Daly analyses, respectively.
[g] Corrected for fractionation, spike, blank, and common Pb. Errors below are 2-sigma. blank Pb: 206Pb/204Pb = 18.271 ± 0.039; 207Pb/204Pb = 15.587 ± 0.095; 208Pb/204Pb = 38.119 ± 0.024. Common Pb values used are from feldspar leaching (Housh and Bowring, 1991; see text). EKC02-51: 206Pb/204Pb = 12.576 ± 0.064; 207Pb/204Pb = 14.042 ± 0.063; 208Pb/204Pb = 32.269 ± 0.060. AGC01-4: 206Pb/204Pb = 12.885 ± 0.001; 207Pb/204Pb = 14.419 ± 0.001; 208Pb/204Pb = 32.572 ± 0.002.
[h] Errors are 2 sigma, propagated using the algorithms of Ludwig (1980).
[i] Calculations are based on the decay constants of Jaffey et al. (1971).
[j] % discordance = 100 - (100 × 206Pb/238U date / 207Pb/206Pb date).

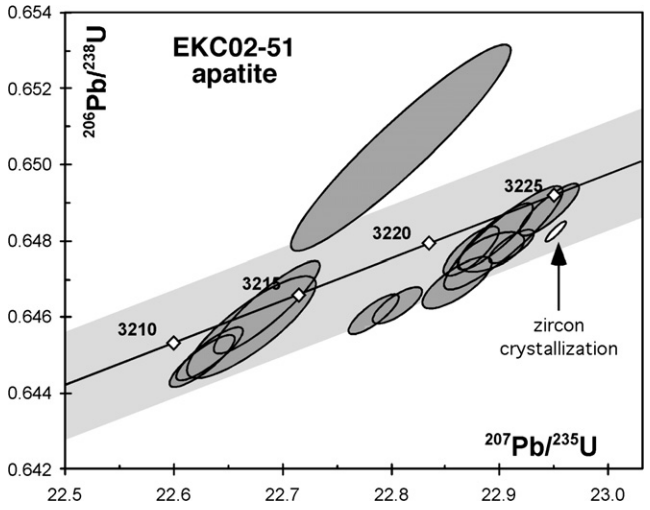

Fig. 4. Concordia diagram for apatite from EKC02-51 (Kaap Valley pluton). Also shown is the weighted mean zircon ellipse from Schoene et al. (2006), reported from the same sample. Gray band is the error envelope for the concordia curve. Errors are at the 95% confidence interval.

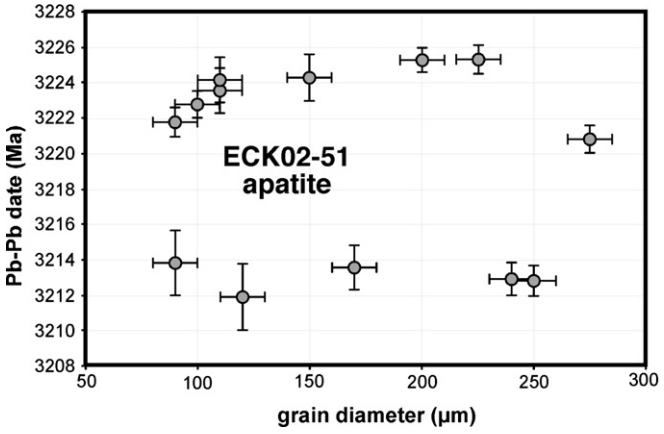

Fig. 5. *a–t* plot for apatite from EKC02-51. Errors on the grain diameter are estimated to be uniformly ±10 μm. Diameter is measured perpendicular to the *c*-axis. Errors are at the 95% confidence interval.

analyzed for U–Pb isotopes (Table 1, Fig. 8). All fractions but one (s7) are within error of concordia, and that fraction is about −6% discordant and will not be discussed further. Three of those twelve (s1, s4, and s6) were air-abraded until they had a distinctly spherical shape. The air-abraded fractions yield consistently old $^{207}Pb/^{206}Pb$ dates from about 3168 to 3171 Ma, while all but two of the remaining unabraded fractions show a trend between grain size and $^{207}Pb/^{206}Pb$ date from about 3140 to 3170 Ma (Fig. 9).

4.2.3. Apatite

Apatite picked from AGC01-4 is clear, non-magnetic and ranges from elongate cylindrical prisms to stubby cylindrical barrels. Larger grain sizes (>150 μm diameter) lack an elongate habit, with typical aspect ratios of ~2, and this distinction appears texturally to be a primary fea-

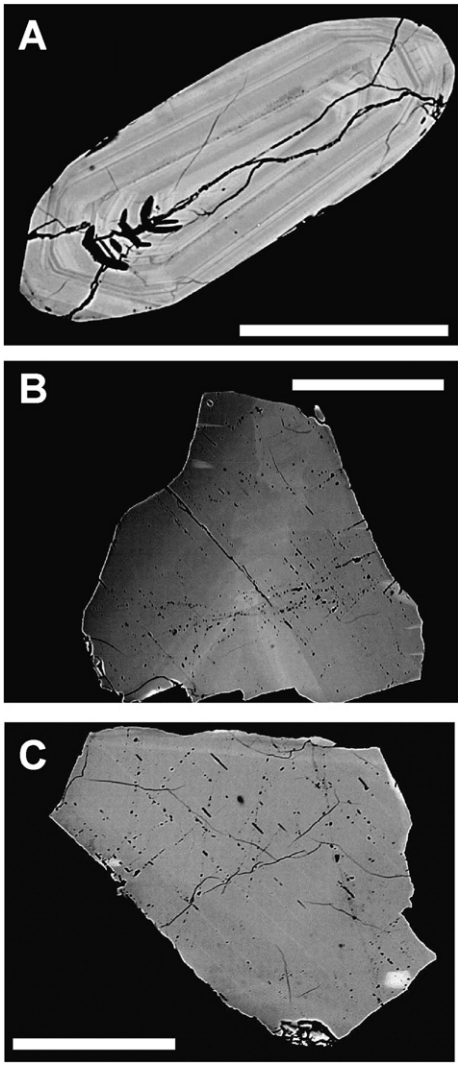

Fig. 6. Back-scattered electron images of typical zircon (A) and titanite (B and C) from AGC01-4. Scale bar in (A) is 50 μm, and in (B) and (C) is 100 μm. Note the concentric oscillatory zoning in the zircon, indicating a magmatic origin. Also note that titanite grains display weak oscillatory zoning and are subhedral, but likely broken during processing.

ture, not a result of rock processing. BSE images show no zoning features, but CL images reveal oscillatory zoning in the cores with overgrowths of variable thickness (Fig. 10). Overgrowths are both bright and dark in CL and cut the internal zoning in places and are concordant to the zoning in others.

Twenty-eight apatite fractions were analyzed for U–Pb systematics (Table 1, Fig. 8). Ten grains were removed from grain mount after imaging (Figs. 8 and 10). In addition, three multi-grain and nine single-grain apatite fractions were analyzed without imaging. All of the analyses are nearly concordant (except for one that is −3% discordant) and give $^{207}Pb/^{206}Pb$ dates that span over 100 Myr from about 3060 to 3170 Ma (Fig. 8). In addition, the analyses show a strong correlation between grain size and $^{207}Pb/^{206}Pb$ date (Fig. 9). Grain size was measured as (1) the width of the cylinder or barrel for single, whole grain analyses (i.e. perpendicular to the *c*-axis), (2) the original width of the cylinder or barrel

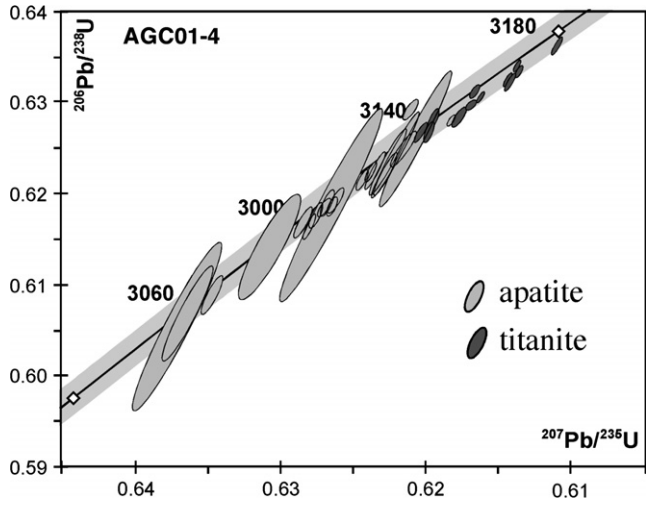

Fig. 8. Concordia diagram for titanite and apatite from AGC01-4. Shaded gray envelope is the error-bounds of the concordia curve. Errors are at the 95% confidence interval.

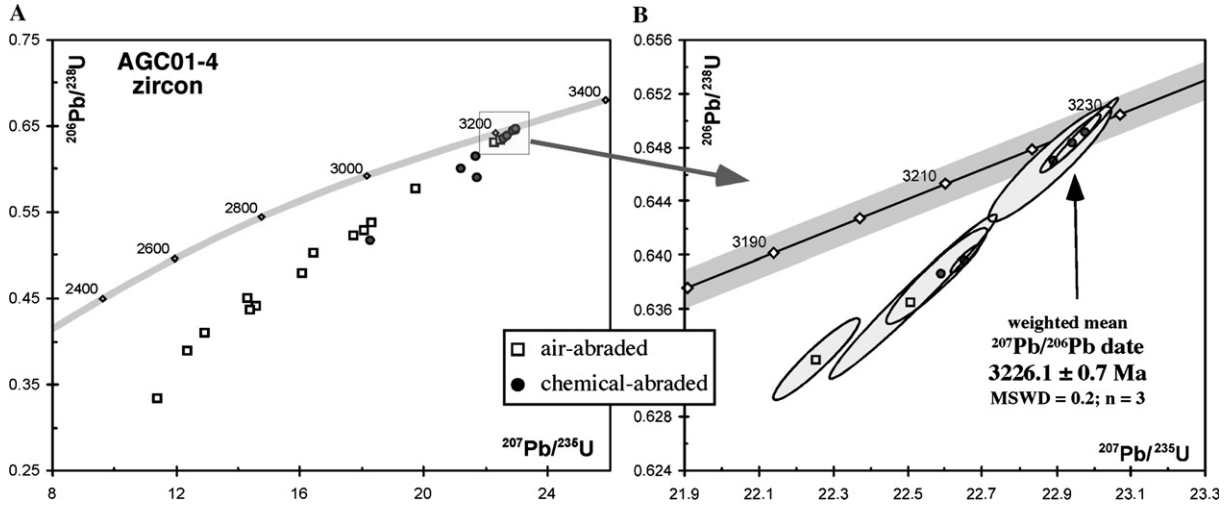

Fig. 7. Concordia diagram for zircon from AGC01-4 depicting both air-abraded and chemical-abraded zircon grains. (B) is blow-up of shaded region in (A). Shaded gray envelope is the error-bounds of the concordia curve. Errors are at the 95% confidence interval.

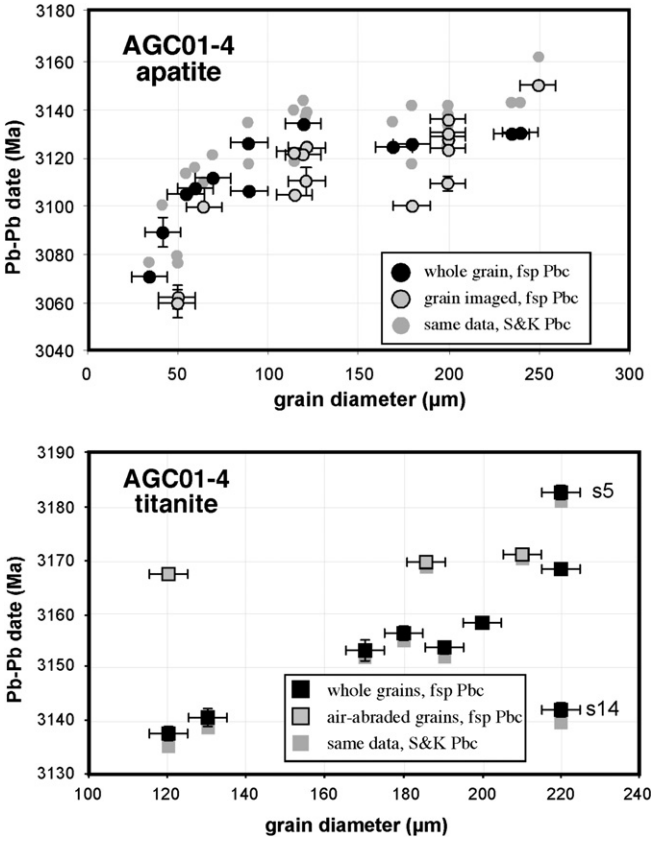

Fig. 9. *a–t* curves for apatite and titanite from AGC01-4. Light gray points (without error bars) represent the data reduced with the Stacey and Kramers (1975) estimate for common Pb (S&K Pb_c), to show the affect of Pb_c choice. See text for further discussion, and see Table 1 caption for Pb_c from feldspar leachates. Errors on grain diameters are uniformly chosen to be ±10 μm. Diameter for apatite was measured perpendicular to the *c*-axis and for titanite is the average of the three principle axes. Errors are at the 95% confidence interval.

as the grain appeared in the EMP image prior to their removal or breaking in grain mount, or (3) the average cylinder width for multi-grain analyses (which were grouped to be roughly the same grain size).

4.3. BSO4-5

This is a sample of the Pigg's Peak granite that intrudes the inlier of ca. 3.2–3.6 Ga basement rocks where AGC01-4 was sampled (Fig. 2). Our sample was collected at the SE margin of the basement inlier near the "falls" outcrop (Compston and Kröner, 1988; Kröner et al., 1989), within several hundred meters from the contact with AGC rocks. It is a medium-grained undeformed biotite granite that clearly post-dates all deformation in the adjacent polymodal gneisses. Zircon from this sample is clear to pink and euhedral with sharp crystal terminations. Five grains were chosen for U–Pb analysis by the chemical-abrasion method (Table 1, Fig. 11). Four of the five grains yield a $^{207}Pb/^{206}Pb$ date of 3140.3 ± 0.3 Ma (MSWD = 0.4), and we interpret this to reflect the local crystallization age of the Pigg's Peak batholith. One grain (za1) falls outside this cluster, and including it in the weighted mean does not effect the age beyond error, but raises the MSWD to 3.2. The outlier may be a result of an older, inherited domain in the grain.

5. Discussion and analysis

5.1. U–Pb thermochronology in an absolute time-frame

Interpreting our U–Pb apatite and titanite data in an absolute time-frame is hampered by potential inaccuracies in the U decay constants and uncertainties in the composition of non-radiogenic Pb (Pb_c). Inaccuracies in the U decay constants are discussed elsewhere (Mattinson, 1994, 2000; Schoene et al., 2006), and introduce a bias of <0.3% between $^{206}Pb/^{238}U$ and $^{207}Pb/^{206}Pb$ dates for rocks ~3 Ga. In this study, we choose to report and compare data within the $^{207}Pb/^{206}Pb$ system alone, using the $^{238}U/^{206}Pb$ and $^{235}U/^{207}Pb$ systems only to evaluate open system behavior. Therefore, any absolute inaccuracy introduced by the U decay constants is systematic and does not jeopardize our ability to quantitatively compare $^{207}Pb/^{206}Pb$ dates. Studies wishing to compare these dates with non-$^{207}Pb/^{206}Pb$ dates need to incorporate decay constant errors (see also Renne et al., 1998; Min et al., 2000; Begemann et al., 2001).

The correction for Pb_c in minerals with low Pb^*/Pb_c is the biggest source of inaccuracy in calculated U–Pb dates. Making the correction to measured ratios can be done in three ways: (1) using a bulk-earth Pb evolution model, such as Stacey and Kramers (1975), (2) using the Pb isotopic composition from cogenetic low-μ phases, such as K-feldspar, and (3) using traditional $^{238}U/^{206}Pb$ and $^{235}U/^{207}Pb$ isochron regressions or the more powerful 3-D total Pb–U isochron (Ludwig, 1998). Isochron methods are not applicable here, given that these data obviously do not meet the required assumption that all the minerals record the same date. We have chosen instead to reduce the data using the K-feldspar step-leaching techniques of Housh and Bowring (1991), taking the values determined from the leach step with the least radiogenic Pb composition as the best estimate of initial Pb (these data are reported in the caption of Table 1). In the case of apatite from EKC02-51 and titanite from AGC01-4 (because of the relatively high Pb^*/Pb_c ratios) the difference in calculated dates between using K-feldspar Pb_c and the Stacey and Kramers (1975) estimate is on average only different by 0.3 and 1.5 Myr, respectively (Figs. 5 and 9). Apatite data from AGC01-4, however, is quite dependent on the choice of Pb_c, and the data are on average ~11 Myr younger with the K-feldspar Pb_c values (Fig. 9). Though numerous studies have shown that this is probably more accurate than using the ad-hoc correction provided by the Stacey and Kramers (1975) Pb curve (Corfu, 1988; Verts et al., 1996; Mezger and Cosca, 1999; Chamberlain and Bowring, 2000; Schmitz and Bowring, 2001), the accuracy of the K-feldspar Pb correction is difficult to verify. For example, Schoene and Bowring (2006) show that U–Pb thermochro-

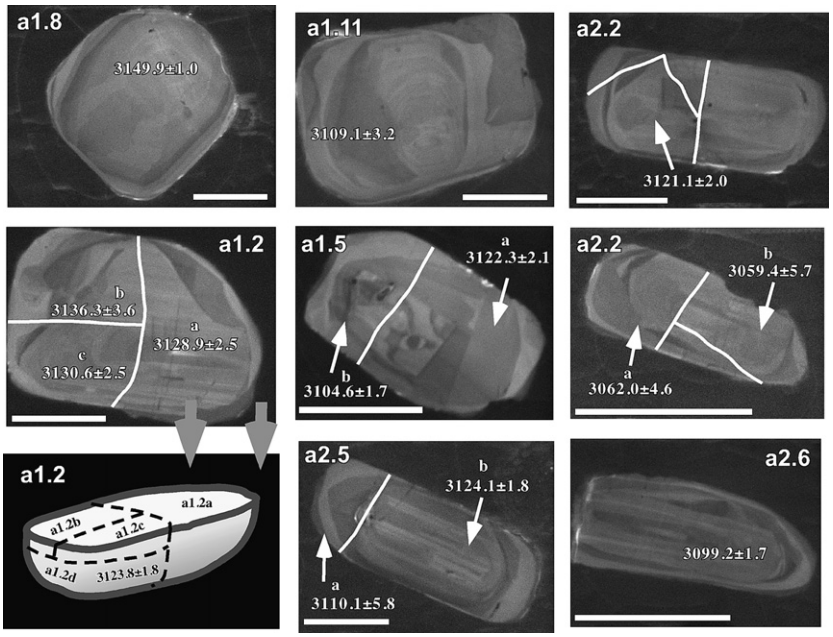

Fig. 10. Cathodoluminescence images of apatite from AGC01-4, with fraction number in top corner. White lines are where grains were broken prior to removal from grain mount, and the corresponding $^{207}Pb/^{206}Pb$ dates are shown. U–Pb data is in Table 1. Note that the lower a1.2 grain is meant to be a 3D depiction of how the grain was fragmented. See text for further discussion. Scale bars are 100 μm. Errors are at the 95% confidence interval.

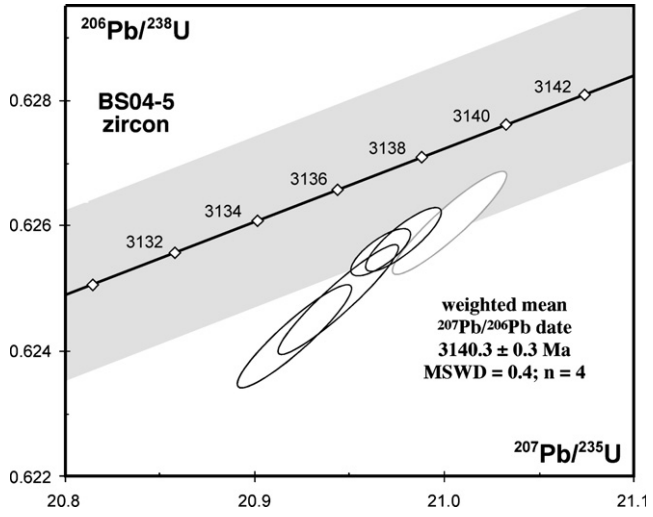

Fig. 11. Concordia diagram for zircon from BS04-5, a granitic sample from the Pigg's Peak batholith. Shaded gray envelope is the error-bounds of the concordia curve. Errors are at the 95% confidence interval.

nometers and K-feldspar in a quickly cooled syenite do not share the same Pb_c composition, and hypothesize that this is due to the exchange of Pb with an isotopically heterogeneous magmatic fluid over their differing closure intervals. The potential for heterogeneous Pb_c compositions within thermochronometers is even more substantial in slowly cooled rocks, simply because of the heightened probability of complicated rock/fluid interactions over longer timescales. Therefore, demonstration of the accuracy of the Pb_c correction in slowly cooled U–Pb thermochronometers remains a problem to be solved. What is important for this study, however, is that no correlation exists between $^{207}Pb/^{206}Pb$ date and Pb^*/Pb_c but instead between apparent age and grain size, and that the topology of this curve does not change with differing Pb_c estimates (Fig. 9). Therefore, the thermal history defined by apatite is robust, though we must be careful when comparing the absolute timing of this history relative to other data.

5.2. Volume diffusion vs. metamorphic growth

Apatite and titanite from two samples examined in this study can be interpreted to record very different thermal histories. AGC01-4 apatite and titanite show a distribution of dates versus grain size that spans over 100 Myr (Figs. 8 and 9), while EKC02-51 apatite from the Kaap Valley pluton fall into two distinct clusters of dates within 15 Myr after crystallization of the pluton (Figs. 4 and 5). Each sample can be used to illustrate fundamental processes controlling U–Pb systematics in these minerals, and will be discussed below.

5.2.1. EKC02-51

Apatite from the Kaap Valley pluton form two populations with distinct $^{207}Pb/^{206}Pb$ dates (Figs. 4 and 5), suggesting two different processes are recorded and can be interpreted in the context of two models: (1) that the older population represents primary igneous apatite that records cooling and the younger one records a period of metamorphic/hydrothermal growth below the T_c of apatite, or (2) that the two populations, because of compositional heterogeneities, have different T_c. Experiments have been published on the diffusion of O (Farver and Giletti, 1989),

Sr (Watson et al., 1985; Cherniak and Ryerson, 1993), REE (Watson et al., 1985; Cherniak, 2000), U and Mn (Cherniak, 2005), anionic halogens such as F, Cl, and OH (Brenan, 1993), and Pb (Watson et al., 1985; Cherniak et al., 1991). We know of no study that looks at compositional effects on the diffusion of Pb in apatite. Cherniak (2000) documented the dependence of trivalent REE diffusion on the method of cation substitution (coupled or non-coupled) in fluorapatite, which in turn depends on the concentration of other mono- to pentavalent cations in the crystal lattice (see summary in Pan and Fleet, 2002). Because Pb^{2+} substitutes directly for Ca^{2+} in the apatite structure, intralattice cation distribution is less likely to affect Pb diffusion, and one may expect any compositional effect on Pb diffusion to be minimal. If the closure temperature of a compositionally distinct generation of apatite was more than ~100 °C lower than the older population, then the apatite dates would reflect a complex history of slow-cooling or reheating, similar to ~3.03–3.14 Ga $^{40}Ar/^{39}Ar$ dates from biotite ($T_c \approx 300$–350 °C; Harrison et al., 1985; Grove and Harrison, 1996) in this pluton (Layer et al., 1992). Whether compositionally variable closure temperatures are represented in these data or not, both options 1 and 2 require the generation of multiple populations of apatite and this deserves discussion.

Numerous natural and experimental studies have documented that apatite is sensitive to variable metamorphic conditions and/or fluid compositions (Korzhinskiy, 1981; Yardley, 1985; Zhu and Sverjensky, 1991; Fleet and Pan, 1997; Fleet et al., 2000), such that intragrain variations in apatite composition can act as a robust indicator of changing metamorphic conditions and/or fluid composition as a function of time. Krenn and Finger (2004) reported both Sr-rich (>33 wt%) apatite armored by garnets and Ca-rich compositions elsewhere in the rock and conclude the Sr-rich varieties preserve apatite equilibrated during high-pressure metamorphism. Grain armoring was also inferred by Loferski and Ayuso (1995), who showed that apatite occurring as multiphase inclusions in clinopyroxene have distinct Cl/(F + Cl + OH) ratios from apatite located within the groundmass. Meurer and Boudreau (1996) and Willmore et al. (2000) investigated apatite halogen composition within the Stillwater and Bushveld layered mafic intrusions, respectively. Each found distinct differences in Cl mole fraction in fluorapatite as a function of stratigraphic height and conclude that this is because the composition of fluids in the rock evolved over time and space during the late-stage magmatic history. These studies exemplify that the composition of apatite within a rock can change as a function of time depending on the degree of rock-fluid interaction; the textural setting of apatite (e.g. degree of armoring) may help determine whether or not it preserves early compositional variations.

Grain armoring may have been important in preserving the two different populations of U–Pb apatite dates recorded in EKC02-51 (Figs. 4 and 5). Petrographic evidence shows that large euhedral apatite exists only along grain boundaries and as inclusions in biotite, and we infer that this population is the euhedral blue colored population in mineral separates. Secondary chlorite, epidote, clinozoisite, and white mica are also associated with euhedral apatite. Only subhedral cylinder to barrel shaped apatite is found as inclusions in quartz and plagioclase. It therefore seems plausible that the older population is represented by grains that are armored by quartz or feldspar and the younger population is associated with metamorphic/hydrothermal processes. Igneous apatite originally located on grain boundaries or otherwise accessible by fluid flow must have been dissolved or recrystallized during secondary apatite growth because there is no evidence of mixing between the two populations. Therefore, chemical equilibration of apatite during metamorphism would have occurred by dissolution/reprecipitation and not diffusion or mineral overgrowth.

5.2.2. AGC01-4

Apatite from AGC01-4 gives $^{207}Pb/^{206}Pb$ dates that span over 100 Myr (Figs. 8 and 9). Such a spread in dates could be the result of mixing portions of grains with different ages, which is supported by CL images that reveal fine-scale oscillatory zoning in cores typically overgrown and/or truncated by rims with broad to patchy zoning (Fig. 10). To test this hypothesis, grains a1.5 and a2.5 were imaged, broken, and removed from grain mount and analyzed for U and Pb in order to isolate portions of the grains near the edge (Fig. 10). Fragments with a proportionally larger amount of material near the grain edge are distinctly younger (i.e. a1.5b is younger than a1.5a and a2.5a is younger than a2.5b; Fig. 10), which is consistent with isotopic zonation from core to rim. In addition, grain a1.2 was microsampled to isolate one of the overgrowths in three dimensions by removing a thin slice of material parallel to the imaged surface (a1.2b; Fig. 10). One would expect that fragment to be distinctly younger than a1.2c if the apparent metamorphic overgrowth occurred after the rock passed below the T_c of apatite. Instead, dates for a1.2b and a1.2c are within error. These observations suggest that there is a gradient in $^{207}Pb/^{206}Pb$ date within the apatites, but that it is not resulting from metamorphic overgrowth. Also, the strong correlation of date with grain size would not be expected from mixing igneous and metamorphic growth zones. We should note that on the *a–t* curve in Fig. 9, the grains which were removed from grain mount all plot slightly below the whole-grain analyses, such that they are slightly younger for a given grain size. This is because when the grains were removed from the mounts, it became apparent that more than 50% of the material was removed during polishing, thereby increasing the proportion of material near the grain edge. These data are best explained by volume diffusion of Pb through the crystal lattice with the grain size as the effective diffusion dimension, as predicted by Dodson (1973, 1986). Because these apatite retain that information, it suggests not only that the grain size is a good proxy for the effective diffusion

dimension, but also that the metamorphic rims observed in CL images grew above the closure temperature of apatite at an unrecorded time.

Titanite from AGC01-4 also show a correlation between $^{207}Pb/^{206}Pb$ date and grain size (Fig. 9). Two of the larger fractions (s5 and s14) deviate from this trend, yielding both older and younger dates and this anomalous behavior may be explained by (1) unrecognized zircon inclusions in the grain, (2) if the picked fractions were not, in fact, whole grains but instead broken shards of once larger grains, or (3) if cracks or metamictization in the grains produced fast-diffusion pathways for Pb-loss. In any case, we regard the *a–t* relationship as robust despite the two outliers. The three grains that were air-abraded to isolate their cores give nearly identical $^{207}Pb/^{206}Pb$ dates of ~3170 Ma regardless of the grain size (grain sizes were measured post-abrasion). As with the apatite, these observations are consistent with titanite that have the grain size acting as the effective diffusion dimension.

5.3. Testing for slow-cooling or reheating with numerical modeling

The interpretation that volume diffusion is the primary control on the measured dates in both apatite and titanite from AGC01-4 implies that significant information about the thermal history of the rock is recorded in these minerals. In the analysis that follows, we use a finite-difference numerical model to explore the predicted closure-times (t) of apatite and titanite as a function of grain size (a) for varying T–t paths to test whether or not a–t curves from multiple thermochronometers are unique indicators of thermal history recorded in AGC01-4. The setup and inputs for our model are presented in Appendix A; only discussions of the particularly important input variables and the results are presented below.

We use the model to test the two ways of generating the observed a–t curves for apatite and titanite: (1) slow-cooling after crystallization of AGC01-4, and (2) fast cooling followed by thermal perturbation. These differing scenarios are shown in Figs. 12–14, with both the model T–t paths and the resulting a–t curves for apatite and titanite. The data from AGC01-4 is plotted for comparison; only whole-grain data is plotted (i.e. non-abraded titanite, non-polished apatite), as the U–Pb systematics in those grains should best approximate volume diffusion.

In the case of slow cooling, it can be shown that a single cooling rate following intrusion can explain both the apatite and the titanite data exclusively, but not both data sets together. Fig. 12 illustrates this point by showing 0.7 °C/Myr (curve 1) and 1.5 °C/Myr (curve 3) linear cooling trajectories, which can fit the a–t curve for titanite and apatite, respectively; neither curve fits both datasets. In order to produce the observed combination of trends, a model that combines slow and fast cooling is necessary, and the best combination is shown in Fig. 12, curve 2. A T–t curve with such topology is necessary not only to explain the nearly

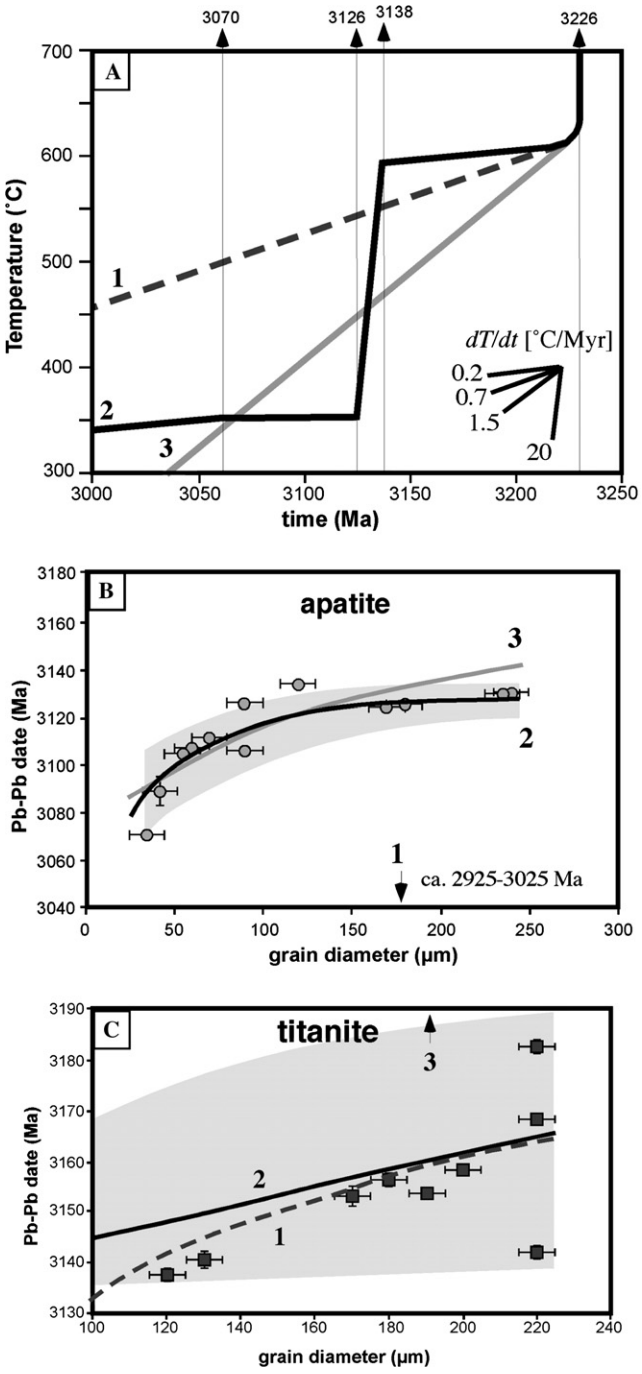

Fig. 12. Results from finite-difference numerical model to test whether slow cooling can explain the observed data from AGC01-4. T–t paths labeled 1, 2, and 3 in (A) correspond to the resulting a–t curves in (B) and (C) for apatite and titanite, respectively. Dates at the top of (A) are when changes in cooling rate occur in curve 2. Note that curve 2 is the optimized scenario, which fits the U–Pb data the best. Shaded regions in (B) and (C) are the error-bounds for the synthetic a–t curve 2. See text for discussion. Errors are at the 95% confidence interval.

overlapping closure times for titanite and apatite, but also to replicate the topology of the apatite data: relatively flat in larger grain sizes, and steepening in smaller grain sizes.

We also tested the possibility that resetting by known magmatic intrusions could have created the observed tita-

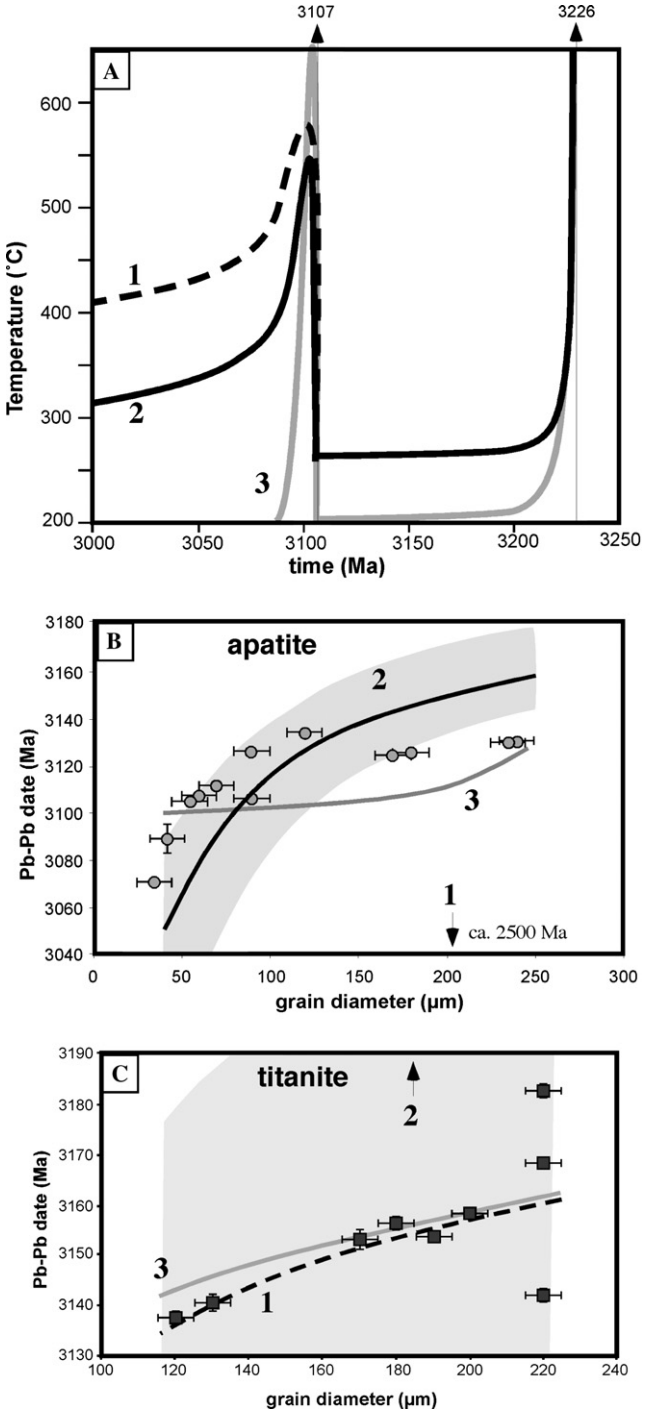

Fig. 13. Results from finite-difference numerical model to test whether thermal resetting of apatite and titanite at 3110 Ma can explain the observed data from AGC01-4. *T–t* paths labeled 1, 2, and 3 in (A) correspond to the resulting *a–t* curves in (B) and (C) for apatite and titanite, respectively. Dates at top of (A) are the dates of crystallization and intrusion of magma that causes the thermal anomaly. Shaded regions in (B) and (C) are the error-bounds for the synthetic *a–t* curves 2 and 1, respectively. See text for discussion. Errors are at the 95% confidence interval.

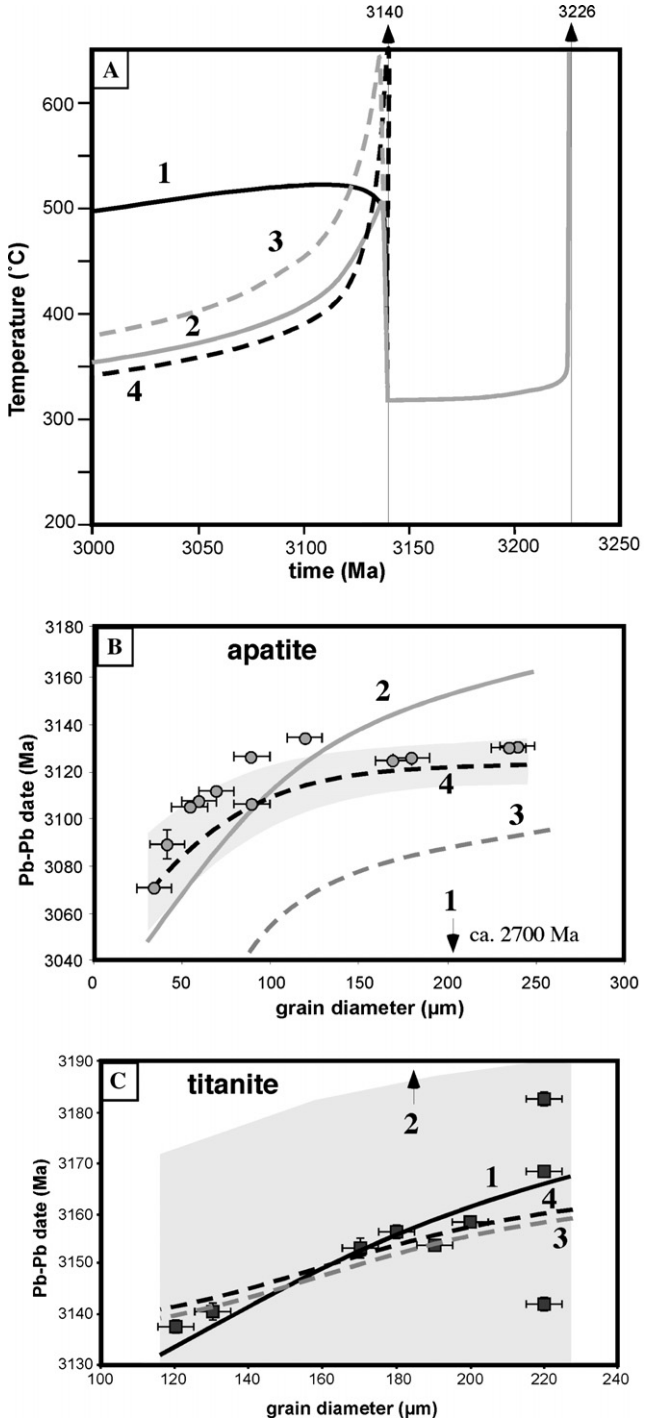

Fig. 14. Results from finite-difference numerical model to test whether thermal resetting of titanite and apatite at 3140 Ma can explain the observed data from AGC01-4. *T–t* paths labeled 1, 2, 3, and 4 in (A) correspond to the resulting *a–t* curves in (B) and (C) for apatite and titanite, respectively. Curves in (A) correspond to intrusions of the following characteristics: 1, 75 km wide, 750 °C; 2, 15 km wide, 750 °C; 3, 12 km wide, 1100 °C; 4, 4.5 km wide, 1360 °C. Gray bands in (B) and (C) are error-bounds for synthetic *a–t* curve 4. See text for discussion. Errors are at the 95% confidence interval.

nite and apatite *a–t* curves. We subjected the model grains to *T–t* paths that initially approximate that of EKC02-51 such that apatite closes several Myr after intrusion, and we then insert a period of reheating at either ~3110 Ma to approximate the intrusion of widespread ca. 3.1 Ga granites into the SE Kaapvaal craton (Fig. 13) or at

~3140 Ma to approximate the effect of the Pigg's Peak granite intrusion dated in this study (Fig. 14). For the ca. 3.1 Ga intrusion, a series of T–t paths were chosen ranging from a lower-temperature thermal perturbation of long duration (curve 1, Fig. 13) to one of higher-temperature but shorter duration (curve 3, Fig. 13). Two scenarios, illustrated by curves 1 and 2 in Fig. 13 can reproduce the titanite and apatite data, respectively, but neither can reproduce both. A high temperature, short duration thermal anomaly can produce model ages similar to both titanite and apatite, but the topology of the model a–t curve for apatite is convex up—opposite of the observed trend. We note that in this analysis the characteristics of the intrusion (i.e. temperature, size, and distance from the sample) are unimportant—no thermal perturbation can reproduce the mineral a–t data.

For a thermal perturbation at ~3140 Ma, the analysis is more sensitive to the duration and magnitude of heating. Fortunately, we know the necessary model inputs from the local geology: the distance from the intrusion margin is known (2 km), the intrusion has been suggested to be tabular and horizontally expansive but only 1–2 km thick (Jackson and Robertson, 1983), and the chemistry of the magma gives a constraint on the temperature. For an ~750 °C granite, it is necessary for the intrusion to be about 75 km wide to reset the modeled titanite to fit the data, and this results in apatite ages that are far too young (Fig. 14, curve 1). The apatite data can be reproduced with a 15 km wide intrusion, but the titanite is not reset at all (Fig. 14, curve 2). To reproduce both apatite and titanite, a short-duration, very high-temperature intrusion is necessary. For example, curve 3 in Fig. 14 corresponds to a 12 km wide, 1100 °C intrusion and curve 4 corresponds to a 4 km wide, 1360 °C intrusion; the latter of which reproduces the data but is an unrealistically high temperature for a granite. Therefore, we conclude that the cooling curve 2 in Fig. 12, which shows two periods of slow cooling interrupted by a period of fast cooling, to be the best fit to our data. The implications of this path for the geology of the Kaapvaal craton will be discussed later in the text.

5.3.1. Model uncertainties

The analysis above focuses on the mean values of the experimental data for Pb diffusion in titanite and apatite of Cherniak (1993) and Cherniak et al. (1991), respectively, though the uncertainties in D_o and E_a are important. Consideration of the uncertainties in D_o and E_a (titanite: D_o is +106%/−51% and E_a is ±3.4%; apatite: errors for D_o are not reported and E_a is ±2.6%) results in considerable uncertainty in the predicted closure times of the modeled grains. These were propagated by reproducing the model run using the maximum error-bounds for D_o and E_a. The results are illustrated by the shaded gray regions in Figs. 12–14 for a single predicted a–t curve. The magnitude of the errors in the predicted t decrease with increasing cooling rate, and therefore for non-linear T–t paths, these errors can affect the topology of the resulting model a–t curve (which is partly responsible for the asymmetry of the error envelopes). Despite the large errors in the predicted titanite closure time, the broad conclusions of the model do not change. For example, in the case of resetting, T–t curve 2 in Fig. 12 is the best estimate for mimicking the a–t curve for apatite data. The predicted a–t curve for titanite plots outside of the field of view in Fig. 12C and the actual data are still far outside the error envelope. Similarly, T–t curve 3 in Fig. 13 can reproduce the titanite data, but the errors in apatite diffusion parameters cannot account for the bad fit of the topology of the predicted a–t curve for apatite. Clearly, our understanding of diffusion of Pb in accessory minerals, and the uncertainties in those values, can only be aided by further experimentation under variably hydrous conditions.

5.4. Future considerations

Because our data show a clear correlation between grain size and closure date, it can be inferred that volume diffusion over the grain diameter is an important process in the transfer of Pb. Despite this observation, our data show scatter beyond the analytical error from an expected idealized a–t curve, suggesting that certain assumptions of the model may not have been fully met in reality. The following sections discuss the relevance of several possible sources of scatter in a–t curves.

5.4.1. Crystal geometry and anisotropy

The preferred T–t path determined above is slightly affected by the choice of diffusion geometry in the minerals. Clearly titanite is not spherical, though it was modeled as such. We regard this assumption to be of minimal importance because as long as the analyzed grains for a given phase are of similar morphology, then the topology of the a–t curve does not change and this can be more important than assumptions of diffusion geometry and therefore the absolute T_c. For example, titanite picked for analysis was as euhedral as possible, and in reality is more ellipsoidal than spherical. Picking small euhedral apatite is trivial because they closely approximate that of perfect cylinders, though larger grains (>150 μm diameter) more closely approximate a barrel or sphere. Deviation from an ideal cylindrical shape in larger grain sizes could affect the topology of the a–t curve (Fig. 15).

A similar concern is that due to the crystal structures of titanite and apatite (monoclinic and hexagonal, respecitvely), one may expect diffusion of Pb to be anisotropic. In the case of apatite, the diffusion data of Cherniak et al. (1991) was measured perpendicular to the c-axis, which is identical to the modeled diffusion direction in a hexagonal crystal. The reported titanite data (Cherniak, 1993) was measured in two crystallographic directions and found to be very similar in each case, suggesting that titanite can be adequately modeled as an isotropic sphere for diffusion of Pb. These points, though probably of minor importance here, stress the need to carefully choose grains analyzed in studies such as this one.

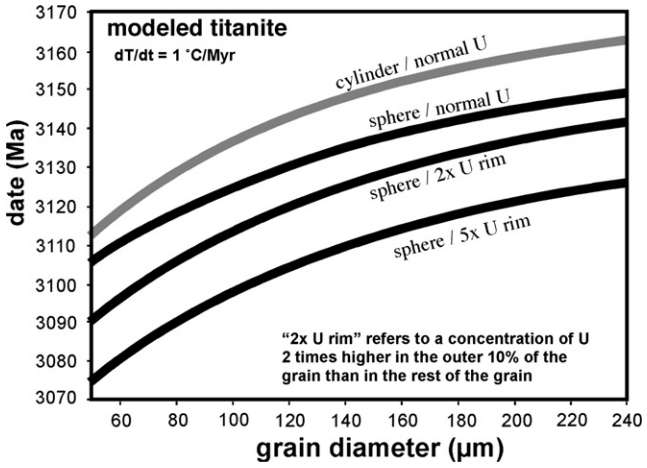

Fig. 15. Results from finite-difference numerical model depicting the affects of the assumed grain geometry and U zonation. Model is run for titanite, which started cooling at 650 °C at 3224 Ma, though it is applicable to any mineral–isotope system. Note that having high U rims on a grain can result in younger ages than with uniform zonation, and can therefore result in scatter in *a–t* curves. See text for further discussion.

5.4.2. Zoning and diffusion of the parent isotope

The mathematical formulation of Dodson (1973, 1986) and the model above assume that the parent isotope (in this case U) is distributed homogeneously throughout the grain and is immobile. The latter assumption is supported by diffusion experiments of uranium in apatite (Cherniak, 2005), which show that uranium diffuses much slower than both Pb and the REE. Because the apatite from AGC01-4 preserve zoning in CL images that is likely the result of REE zoning (e.g. Waychunas, 2002), uranium diffusion is likely unimportant in these grains. More important is that chemical zonation of the parent can affect the closure date of a mineral, which has been acknowledged in U–Th/He dating (Boyce and Hodges, 2005), but thus far has not been treated in the U–Pb system. Complex zonation in apatite with respect to REE, Y, Si and the halogens have been documented (Jolliff et al., 1989; Rakovan and Reeder, 1994; Bingen et al., 1996; Rakovan et al., 1997; Bea and Montero, 1999), and zonation with respect to U and Th have also been reported (Boyce and Hodges, 2005). Such zonation is most important for whole-grain Pb/U analysis if high-U zones exist near the grain edge. Fig. 15 illustrates this point using results from our model in which high U concentrations were placed in the outer 10% of the grain radius, and these models yield anomalously low calculated ages (Fig. 15). Because high-U rims in accessory minerals are commonplace, this effect may help explain the observed scatter in *a–t* curve in AGC01-4 (Fig. 9).

5.4.3. Boundary conditions

Our model imposes a zero concentration boundary condition for Pb^* on the grain margins (see Appendix A), which in reality assumes that the grains are encased in an infinite reservoir of constant Pb concentration and isotopic composition. In reality, diffusion across the boundary of the thermochronometer will be dictated by the partition coefficient for Pb (as a function of temperature) between the grain (e.g. titanite or apatite) and the adjacent phase(s), which cannot be inferred using bulk sample crushing. In the worst-case scenario, the mineral would be entirely encased in a phase with very slow diffusion of Pb, such as garnet or zircon, and therefore prevent escape of Pb and raise the effective T_c. Remedying this problem by establishing petrographic context prior to ID-TIMS U–Pb analysis is not likely to be useful given the difficult necessity of recovering whole or half grains for quantitative thermochronology. In situ U–Pb analysis of apatite, for example by SIMS, is not likely to be useful for establishing *a–t* curves or characterizing intragrain age gradients because of large errors on individual $^{207}Pb/^{206}Pb$ dates (e.g. ±30–100 Myr in Paleoproterozoic grains; Sano et al., 1999). Given the composition of AGC01-4 (tonalitic), it is likely that all the minerals analyzed were either located along grain boundaries or included in feldspar or quartz. No diffusion studies of Pb in quartz have been published, but the T_c of Pb in feldspar is likely similar to that of apatite (Cherniak, 1995) and would not restrain diffusion of Pb^* across its grain boundary. Therefore, while this may affect closure dates of some of the minerals, the robustness of the *a–t* curves suggests it is of minimal concern. The more important effect of matrix composition is in the Pb_c correction, as discussed above.

5.5. Implications for the geology of the SE Kaapvaal craton

The precisely constrained cooling histories from NW and SE of the Barberton Greenstone Belt (BGB), represented by samples EKC02-51 and AGC01-4, respectively, show that rocks on either side of the belt experienced drastically different cooling histories between ca. 3.2 and 3.1 Ga (Figs. 2 and 16). Layer et al. (1992) documented fast cooling in the Kaap Valley pluton in the $^{40}Ar/^{39}Ar$ systematics of hornblende and biotite (Fig. 16), and interpreted those data to represent emplacement of the pluton to mid-crustal depths, followed by a variable thermal effect of ca. 3.1 Ga granites depending on sample locality. Our U–Pb apatite data from the Kaap Valley pluton are consistent with those data.

The model cooling path determined above for AGC01-4 (Figs. 12 and 16) can be interpreted as follows: (1) emplacement of granodiorite into the middle- to lower-crust, where it resided for ~80 Myr, (2) exhumation to the middle to upper crust coincident with intrusion of the Pigg's Peak batholith ca. 3140 Ma, and (3) slow-cooling during thermal equilibration of the BGB after the period of 3.1 Ga granitic intrusion. Modeling studies have shown that differential cooling paths in adjacent terranes can be strongly controlled by differential heat production by varying concentrations of U, Th, and K (Royden, 1993; Huerta et al., 1996; Flowers et al., 2004, 2005). However, such models cannot account for the period of rapid cooling evident in AGC01-4. The sharp changes in the cooling rates must

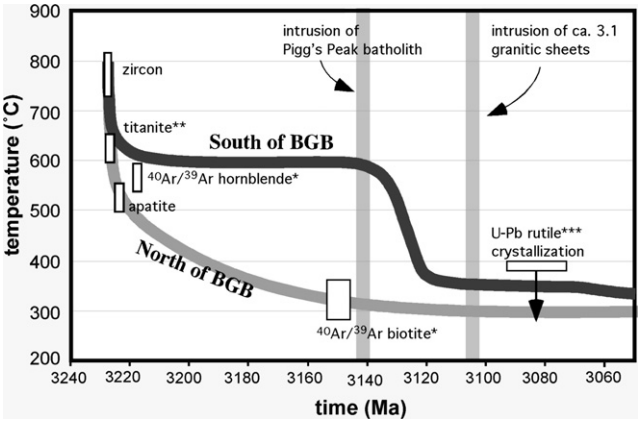

Fig. 16. *T–t* curves from the Kaap Valley pluton (north of the BGB) and from the Ancient Gneiss Complex inlier (south of the BGB). See Fig. 2 for sample localities. South of the BGB curve is that determined from titanite and apatite data from this study in conjunction with numerical modeling (see Figs. 12–14 and the text for discussion). Zircon dates for the Kaap Valley pluton come from Kamo and Davis (1994) and Schoene et al. (2006). ***Data from de Ronde et al. (1991). **Data from Kamo and Davis (1994). *Data from Layer et al. (1992).

be due to some combination of tectonic and erosional processes. In this case, assuming a linear geotherm between 15 and 35 °C/km gives exhumation rates between 1.3 and 0.6 mm/yr for the 12 Myr period of ~20 °C/Myr cooling in AGC01-4. If exhumation were due entirely to erosion (and the geotherm was constant over time), these rates would be reasonable for areas of moderate topography (e.g. Burbank, 2002). This translates into 7–16 km of vertical exhumation over 12 Myr of rapid cooling for the stated geotherms, and requires a major modification of crustal structure.

Attaching a tectonic impetus to the observed exhumation is difficult because geochronologic constraints on tectonic activity after ~3.2 Ga are rare. The necessary period of exhumation along the eastern margin of the BGB begins at the time of the intrusion of the Pigg's Peak batholith ca. 3140 Ma and prior to the intrusion of the ca. 3107 Ga Mpuluzi and Nelspruit batholiths to the south and north of the BGB (Fig. 2). It is widely documented that following ca. 3.23 Ga convergence and thrust-faulting within the greenstone belt, the primary kinematics of the area switched to transtension and extension (Jackson et al., 1987; de Ronde and de Wit, 1994; de Ronde and Kamo, 2000). A proposed mechanism for this transition is extensional collapse of the ca. 3.23 Ga orogen (Jackson et al., 1987; de Ronde and de Wit, 1994; Kamo and Davis, 1994; Kisters et al., 2003), though the timing is poorly constrained. De Ronde et al. (1991) document movement on one such shear zone in the BGB near the Kaap Valley pluton to have occurred between 3126 ± 21 and 3084 ± 18 Ma by dating zircon and rutile from a syntectonic porphyry. It seems likely then, given the current geologic constraints, that the exhumation inferred from our data and modelling is connected to the observed transtension of the crust. The resulting crustal thinning may be responsible for induced heating and melting in the lower crust and the production of the Pigg's Peak batholith to the SE and the ca. 3.1 Ga granites elsewhere. Detailed mapping has revealed that along the borders of the Mpuluzi batholith, the rocks intruded into transcurrent shear zones (Westraat et al., 2005), consistent with this interpretation. When movement on these shear zones stopped is unclear, though our data suggest that significant horizontal thermal gradients existed across the BGB for at least 50 Myr after granitoid intrusion, indicated by the youngest apatite age in AGC01-4 compared to that in the Kaap Valley pluton. Thus, the U–Pb thermochronology reported in this study record both differential exhumation across the BGB ca. 3.2–3.1 Ga and also track the thermal imprint left by granitic intrusion during cratonization ca. 3.1–3.0 Ga.

Acknowledgments

The authors thank J. Ganguly, S. Kamo, and W.E. Hames for helpful reviews of the manuscript. Comments on an early version of the manuscript by J.P. Matzel, and general insight as well as assistance with the numerical modeling from J.W. Boyce are also gratefully acknowledged. Comments on the manuscript, prolonged discussions about the geology of the SE Kaapvaal craton, and invaluable logistical support in the field from M.J. de Wit are continually appreciated.

Associate editor: Yuri Amelin

Appendix A. Finite-difference model setup

To model the diffusion of Pb within apatite and titanite, we use a one-dimensional forward-time center-space finite difference code based on the 1D diffusion equation:

$$\frac{\partial C}{\partial t} = D(T,t)\frac{\partial^2 C}{\partial x^2},$$

in which C is the concentration of Pb [moles/m], t is time [s], and x is the radial distance from the grain's center [m]. D, the diffusion coefficient [m^2/sec], is subject to the Arhenius relationship:

$$D = D_o \exp\left[\frac{-E_a}{RT(t)}\right].$$

Values for D_o and E_a for titanite and apatite were measured experimentally by Cherniak (1993) and Cherniak et al. (1991), respectively, R is the gas constant [J/mole/K], and $T(t)$ is temperature [K] as a function of time [s]. *T–t* curves were constructed by (1) using conjoined segments of linear dT/dt of various durations, or (2) a combination of linear cooling and exponential cooling/reheating that was approximated using the error function solution to the diffusion equation for intrusions of various widths (Carslaw and Jaeger, 1959; Royden, 1993; Turcotte and Schubert, 1982).

Modeled minerals were generated over varying grain radii with a set number of nodes across the radius of each grain. The parent isotope was assigned a concentration for each node along the radius of the grain and allowed to generate daughter product as a function of time. The parent was not allowed to diffuse, and the daughter was allowed to diffuse according the above equations. The concentration of daughter at the grain edge was held constant at zero, mimicking a homogeneous infinite reservoir. Closure ages for minerals are determined by calculating the apparent age at each node based on the ratio of parent to daughter, and to approximate the 3D nature of the problem, each node age was integrated over the appropriate volume depending on the diffusion geometry assumed (i.e. sphere for titanite or cylinder for apatite). Stability of the model was maintained by adjusting the length of a time step based on the T of that time step for a given node spacing, based on the relationship $dt = stability * dx^2/D$. The relationship between the predicted T_c and the variables dx (as determined by the # of nodes) and stability is shown in Fig. A1; also shown is the T_c predicted analytically by Dodson (1986). Based on these curves, stability was held at 0.2 for the model runs and 100 nodes were used in each grain. The results from the modeled titanite agree very well with that predicted by Dodson (1986) in that T_c from our model agree to within 8 °C for cooling rates of <1 °C/Myr and ~5 °C for cooling rates of 10 °C/Myr (Fig. A2) using a spherical geometry. Agreement is even better for cylindrical geometries. The discrepancy between the apparent T_c likely resides in the fact that the Dodson formulation becomes inaccurate at low cooling rates (Dodson, 1973, 1986). Note that in the example here, the grain size and cooling rate are small enough such that the Dodson (1986) formulation is not restricted by diffusive isolation of grain cores (see Ganguly and Tirone, 1999).

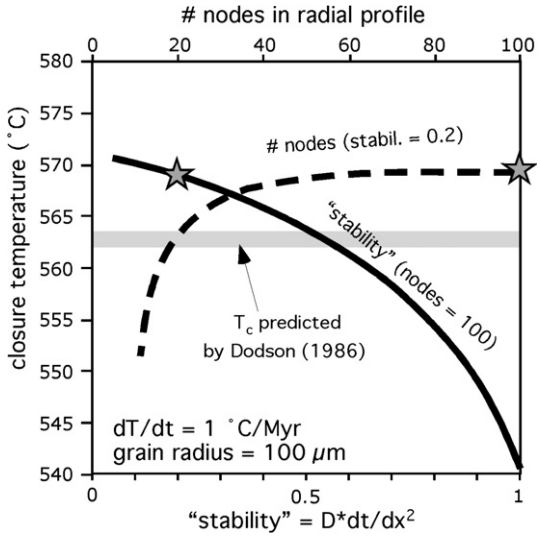

Fig. A1. Stability test of numerical model, comparing results from this model the analytical solution of Dodson (1986) for spherical titanite. See text for discussion.

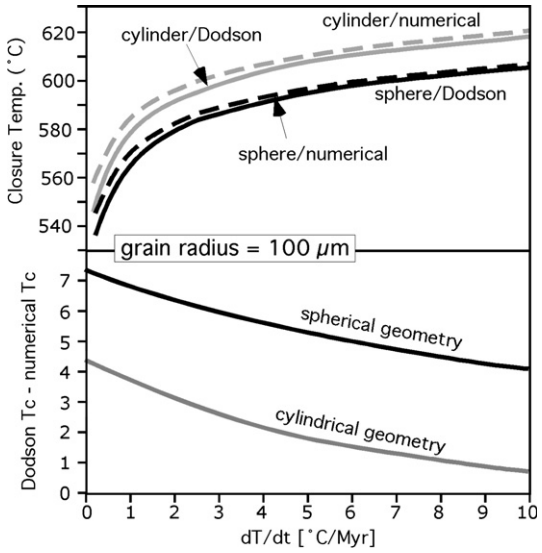

Fig. A2. Quantitative comparison of spherical titanite T_c estimates from the numerical model used in this study to that of Dodson (1986) for a given cooling scenario. See text for discussion.

Therefore, we regard the strong agreement between the analytical and numerical approaches to indicate that our results are robust within the stated assumptions.

References

Aleinikoff, J.N., Wintsch, R.P., Fanning, C.M., Dorais, M.J., 2002. U–Pb geochronology of zircon and polygenetic titanite from the Glastonbury Complex, Connecticut, USA: an integrated SEM, EMPA, TIMS, and SHRIMP study. *Chem. Geol.* **188**, 125–147.

Anhaeusser, C.R., 1969. *The Stratigraphy, Structure, and Gold Mineralization of the Jamestown and Sheba Hills Areas of the Barberton Mountain Land*. University of Witwatersrand, Johannesburg, 332 p.

Anhaeusser, C.R., 1976. The geology of the Sheba HIlls area of the Barberton Mountain Land, South Africa, with particular references to the Eureka syncline. *Geol. Soc. S. Afr. Trans.* **79**.

Anhaeusser, C.R., Robb, L.J., Viljoen, M.J., 1981. Provisional geological map of the Barberton Greenstone Belt and surrounding granitic terrane, Eastern Transvaal and Swaziland. Scale 1:125,000. *Geol. Soc. S. Afr.*.

Armstrong, R.A., Compston, W., de Wit, M.J., William, I.S., 1990. The stratigraphy of the 3.5–3.2 Ga Barberton Greenstone Belt revisited: a single zircon ion microprobe study. *Earth Planet. Sci. Lett.* **101**, 90–106.

Bea, F., Montero, P., 1999. Behavior of accessory phases and redistribution of Zr, REE, Y, Th, and U during metamorphism and partial melting of metapelites in the lower crust: an example from the Kinzigite Formation of Ivrea-Verbano, NW Italy. *Geochim. Cosmochim. Acta* **63**, 1133–1153.

Begemann, F., Ludwig, K.R., Lugmair, G.W., Min, K., Nyquist, L.E., Patchett, P.J., Renne, P.R., Shih, C.-Y., Villa, I.M., Walker, R.J., 2001. Call for an improved set of decay constants for geochronological use. *Geochim. Cosmochim. Acta* **65**, 111–121.

Bingen, B., Demaiffe, D., Hertogen, J., 1996. Redistribution of rare earth elements, thorium, and uranium over accessory minerals in the course of amphiblite to granulite facies metamorphism: the role of apatite and monazite in orthogneiss from southwestern Norway. *Geochim. Cosmochim. Acta* **60**, 1342–1354.

Boyce, J.W., Hodges, K.V., 2005. U and Th zoning in Cerro de Mercado (Durango, Mexico) fluorapatite: insights regarding the impact of recoil distribution of radiogenic ^{4}He on (U–Th)/He thermochronology. *Chem. Geol.* **219**, 261–274.

Brenan, J., 1993. Kinetics of fluorine, chlorine, and hydroxyl exchange in fluorapatite. *Chem. Geol.* **110**, 195–210.

Burbank, D.W., 2002. Rates of erosion and their implications for exhumation. *Miner. Mag.* **66**, 25–52.

Byerly, G.R., Kröner, A., Lowe, D.R., Todt, W., Walsh, M.M., 1996. Prolonged magmatism and time sontraints for sediment deposition in the early Archean Barberton greenstone belt: evidence from the Upper Onverwacht and Fig Tree groups. *Precambrian Res.* **78**, 125–138.

Carslaw, H.S., Jaeger, J.C., 1959. *Conduction of heat in solids*. Oxford University Press, Oxford, 510 p.

Chamberlain, K.R., Bowring, S.A., 2000. Apatite–feldspar U–Pb thermochronometer: a reliable mid-range (~450 °C), diffusion controlled system. *Chem. Geol.* **172**, 173–200.

Cherniak, D.J., 1993. Lead diffusion in titanite and preliminary results on the effects of radiation damage on Pb transport. *Chem. Geol.* **110**, 177–194.

Cherniak, D.J., 1995. diffusion of Pb in plagioclase and K-feldspar investigated using Rutherford backscatter and resonant nuclear reaction analysis. *Contrib. Miner. Petrol.* **120**, 358–371.

Cherniak, D.J., 2000. Rare earth element diffusion in apatite. *Geochim. Cosmochim. Acta* **22**, 3871–3885.

Cherniak, D.J., 2005. Uranium and manganese diffusion in apatite. *Chem. Geol.* **219**, 297–308.

Cherniak, D.J., Lanford, W.A., Ryerson, F.J., 1991. Lead diffusion in apatite and zircon using ion implantation and Rutherford Backscattering techniques. *Geochim. Cosmochim. Acta* **55**, 1663–1673.

Cherniak, D.J., Ryerson, F.J., 1993. A study of strontium diffusion in apatite using Rutherford backscattering spectroscopy and ion implantation. *Geochim. Cosmochim. Acta* **57**, 4653–4662.

Cherniak, D.J., Watson, E.B., 2001. Pb diffusion in zircon. *Chem. Geol.* **172**, 5–24.

Cloete, M., 1991. An overview of metamorphism in the Barber ton greenstone belt. In: Ashwal, L.D. (Ed.), Two Cratons and an Orogen—Excursion Guidebook and Review Articles for a Field Workshop through Selevted Archean Terranes of Swaziland, South Africa and Zimbabwe: Johannesburg, IGCP project 280. Department of Geology, University Witwatersrand.

Compston, W., Kröner, A., 1988. Multiple zircon growth within early Archean tonalitic gneiss from the Ancient Gneiss Complex, Swaziland. *Earth Planet. Sci. Lett.* **87**, 13–28.

Condie, K.C., Macke, J.E., Reimer, T.O., 1970. Petrology and geochemistry of early Precambrian graywackes from the Fig Tree Group, South Africa. *Geol. Soc. Am. Bull.* **81**, 2759–2776.

Corfu, F., 1988. Differential response of U–Pb systems in coexisting accessory minerals, Winnepeg River Subprovince, Canadian Shield: implications for Archean crustal growth and stabilization. *Contrib. Mineral. Petrol.* **98**, 312–325.

Corfu, F., Hanchar, J.M., Hoskin, P.W.O., Kinny, P., 2003. Atlas of zircon textures. In: Hanchar, J.M., Hoskin, P.W.O. (Eds.), *Zircon: Reviews in Mineralogy and Geochemistry*, v. 53. Mineralogical Society of America, Washington, DC, pp. 468–500.

Corfu, F., Stone, D., 1998. The significance of titanite and apatite U–Pb ages: constraints for the post-magmatic thermal-hydrothermal evolution of a batholithic complex, Berens River area, northwestern Superior Province, Canada. *Geochim. Cosmochim. Acta* **62**, 2979–2995.

Dahl, P.S., 1997. A crystal-chemical basis for Pb retention and fission-track annealing systematics in U-bearing minerals, with implications for geochronology. *Earth Planet. Sci. Lett.* **150**, 277–290.

de Ronde, C.E.J., de Wit, M.J., 1994. Tectonic history of the Barberton Greenstone Belt, South Africa: 490 million years of Archean crustal evolution. *Tectonics* **13**, 983–1005.

de Ronde, C.E.J., Kamo, S., 2000. An Archean arc-arc collisional event: a short-lived (*ca.* 3 Myr) episode, Weltevreden area, Barberton greenstone belt, South Africa. *J. Afr. Earth Sci.* **30**, 219–248.

de Ronde, C.E.J., Kamo, S., Davis, D.W., de Wit, M.J., Spooner, E.T.C., 1991. Field, geochemical and U–Pb isotopic constraints from hypabyssal felsic intrusions within the Barberton greenstone belt, South Africa: implications for tectonics and the timing of gold mineralization. *Precambrian Res.* **1991**, 261–280.

de Wit, M.J., 1982. Gliding and overthrust nappe tectonics in the Barberton greenstone belt. *J. Struct. Geol.* **4**, 117–136.

de Wit, M.J., Hart, R.A., Hart, R.J., 1987. The Jamestown ophiolite complex, Barberton mountain belt; a section through 3.5 Ga oceanic crust. *J. Afr. Earth Sci.* **6**, 681–730.

Diener, J.F.A., Stevens, G., Kisters, A.F.M., Poujol, M., 2005. Metamorphism and exhumation of the basal parts of the Barberton greenstone belt, South Africa: Constraining the rates of Mesoarchean tectonism. *Precambrian Res.* **143**, 87–112.

Dodson, M.H., 1973. Closure temperature in cooling geochronological and petrological systems. *Contrib. Miner. Petrol.* **40**, 259–274.

Dodson, M.H., 1975. Kinetic processes and thermal history of rocks. *Carnegie Inst. Yearbook* **74**, 210–217.

Dodson, M.H., 1986. Closure profiles in cooling systems. *Mater. Sci. Forum* **7**, 145–154.

Ducea, M.N., Ganguly, J., Rosenburg, E.J., Patchett, P.J., Cheng, W., Isachsen, C., 2003. Sm–Nd dating of spatially controlled domains of garnet single crystals: a new method of high-temperature thermochronology. *Earth Planet. Sci. Lett.* **213**, 31–42.

Dunlap, W.J., Kronenberg, A.K., 2001. Argon loss during deformation of micas: constraints from laboratory deformation experiments. *Contrib. Miner. Petrol.* **141**, 174–185.

Dziggel, A., Stevens, G., Poujol, M., Anhaeusser, C.R., Armstrong, R.A., 2002. Metamorphism of the granite–greenstone terrane south of the Barberton Greenstone Belt, South Africa: an insight into the tectonothermal evolution of the 'lower' portions of the Onverwacht Group. *Precambrian Res.* **114**, 221–247.

Eriksson, K.A., 1980. Transitional sedimentation stules in the Moodies and Fig Tree Groups, Barberton Mountain Land, South Africa: evidence favouring an Archean continental margin. *Precambrian Res.* **12**, 141–160.

Farver, J.R., Giletti, J., 1989. Oxygen and strontium diffusion kinetics in apatite and potential applications to thermal history determinations. *Geochim. Cosmochim. Acta* **53**, 1621–1631.

Fleet, M.E., Liu, X., Pan, Y., 2000. Rare-earth elements in chlorapatite $[Ca_{10}(PO_4)_6Cl_2$: uptake, site preference, and degredation of monoclinic structure. *Amer. Mineral.* **85**, 1437–1446.

Fleet, M.E., Pan, Y., 1997. Site preference of rare earth elements in fluorapatite: Binary (LREE + HREE)-substituted crystals. *Am. Mineral.* **82**, 870–877.

Flowers, R.M., Royden, L.H., Bowring, S.A., 2004. Isostatic constraints on the assembly, stabilization, and preservation of cratonic lithosphere. *Geology* **32**, 321–324.

Flowers, R.M., Royden, L.H., Bowring, S.A., 2005. Isostatic constraints on lithospheric thermal evolution: Application to the Proterozoic orogen of the southwestern, U.S. In: Karlstrom, K.E., Keller G.R. (Eds.), Geophysical Monograph Series: Lithospheric structure and evolution of the Rocky Mountain region, v. 154.

Franz, G., Spear, F.S., 1985. Aluminous titanite (sphene) from the eclogite zone, South-central Tauern Window, Austria. *Chem. Geol.* **50**, 33–46.

Frost, B.R., Chamberlain, K.R., Schumacher, J.C., 2000. Sphene (titanite): phase relations and role as a geochronometer. *Chem. Geol.* **172**, 131–148.

Ganguly, J., Tirone, M., 1999. Diffusion closure temperature and age of a mineral with arbitrary extent of diffusion: theoretical formulation and applications. *Earth Planet. Sci. Lett.* **170**, 131–140.

Ganguly, J., Tirone, M., Hervig, R., 1998. Diffusion kinetics of samarium and neodymuim in garnet, and a method of determining cooling rates of rocks. *Science* **281**, 805–807.

Gerstenberger, H., Haase, G., 1997. A highly effective emitter substance for mass spectrometric Pb isotope ratio determinations. *Chem. Geol.* **136**, 309–312.

Gromet, L.P., 1991. Direct dating of deformational fabrics, Short Course Handbook on Applications of Radiogenic Isotope Systems to Problems in Geology. *Mineralogical Association of Canada*, 167–189.

Grove, M., Harrison, T.M., 1996. $^{40}Ar^{*}$ diffusion in Fe-rich biotite. *Am. Mineral.* **81**, 940–951.

Harrison, T.M., 1981. Diffusion of ^{40}Ar in hornblende. *Contrib. Miner. Petrol.* **78**, 324–331.

Harrison, T.M., Duncan, I., McDougall, I., 1985. Diffusion of ^{40}Ar in biotite; temperature, pressure and compositional effects. *Geochim. Cosmochim. Acta* **49**, 2461–2468.

Hawkins, D.P., Bowring, S.A., 1999. U–Pb monzaite, xenotime and titanite geochronological constraints on the prograde to post-peak metamorphic thermal history of Paleoproterozoic migmatites from the Grand Canyon, Arizona. *Contrib. Mineral. Petrol.* **134**, 150–169.

Heubeck, C., Lowe, D.R., 1994. Late syndepositional deformation and detachment tectonics in the barberton Greenstone Belt, South Africa. *Tectonics* **13**, 1514–1536.

Hodges, K.V., 2003. Geochronology and thermochronology in orogenic systems. *Treatise Geochem.* **3**, 263–292.

Housh, T., Bowring, S.A., 1991. Lead isotopic heterogeneities within alkali feldspars: implications for the determination of initial lead isotopic compositions. *Geochim. Cosmochim. Acta* **55**, 2309–2316.

Huerta, A.D., Royden, L.H., Hodges, K.V., 1996. The interdependence of deformational and thermal processes in mountain belts. *Science* **273**, 637–639.

Hunter, D.R., Barker, F., Millard, H.T., 1978. The geochemical nature of the Archean Ancient Gneiss Complex and granodiorite suite, Swaziland: a preliminary study. *Precambrian Res.* **7**, 105–127.

Jackson, M.P.A., 1979. High-strain deformation of the Ancient Gneiss Complex in the Mankayane area, Swaziland: a preliminary account (abstr.). *Geol. Soc. S. Afr.—18th congress* **1**, 210–216.

Jackson, M.P.A., 1984. Archean structural styles in the Ancient Gneiss Complex of Swaziland, southern Africa. In: Kröner, A., Greiling, R. (Eds.), *Precambrian Tectonics Illustrated*. Schweizerbart'sche Verlagsbuchhandlung, Stuttgart, pp. 1–18.

Jackson, M.P.A., Eriksson, K.A., Harris, C.W., 1987. Early Archean foredeep sedimentation related to crustal shortening: a reinterpretation of the Barberton Sequence, southern Africa. *Tectonophysics* **136**, 197–221.

Jackson, M.P.A., Robertson, D.I., 1983. Regional implications of early-Precambrian strains in the Onverwacht Group adjacent to the Lochiel Granite, northwest Swaziland. In: Anhaeusser, C.R. (Ed.), Contributions to the geology of the Barberton Mountain Land, v. 9. Geol. Soc. S. Afr., Spec. Publ., pp. 45–62.

Jolliff, B.L., Papike, J.J., Shearer, C.K., Shimizu, N., 1989. Inter- and intra-crystal REE variations in apatite from the Bob Ingersoll Pegmatite, Black Hills, South Dakota. *Geochim. Cosmochim. Acta* **53**, 429–441.

Kamo, S., Davis, D.W., 1994. Reassessment of Archean crustal development in the Barberton Mountain Land, South Africa, based on U–Pb dating. *Tectonics* **13**, 167–192.

Ketchum, J.W.F., Heaman, L.M., Krogh, T.E., Culshaw, N.G., Jamieson, R.A., 1998. Timing and thermal influence of late orogenic extension in the lower crust: a U–Pb geochronological study from the southwest Grenville orogen, Canada. *Precambrian Res.* **89**, 25–45.

Kisters, A.F.M., Anhaeusser, C.R., 1995. Emplacement features of Archean TTG plutons along the southern margin of the Barberton greenstone belt, South Africa. *Precambrian Res.* **75**, 1–15.

Kisters, A.F.M., Stevens, G., Dziggel, A., Armstrong, R.A., 2003. Extensional detachment faulting and core-complex formation in the southern Barberton granite–greenstone terrain, South Africa: evidence for a 3.2 Ga orogenic collapse. *Precambrian Res.* **127**, 335–378.

Korzhinskiy, M.A., 1981. Apatite solid solutions as indicators of the fugacity of HCl and HF in hydrothermal fluids. *Geochem. Intl.* **3**, 45–60.

Krenn, E., Finger, F., 2004. Metamorphic formation of Sr-apatite and Sr-bearing monazite in a high-pressure rock from teh Bohemian Massif. *Am. Mineral.* **89**, 1323–1329.

Krogh, T.E., 1973. A low contamination method for hydrothermal decomposition of zircon and extraction of U and Pb for isotopic age determination. *Geochim. Cosmochim. Acta* **37**, 485–494.

Krogh, T.E., 1982. Improved accuracy of U–Pb zircon ages by the creation of more concordant systems using an air abrasion technique. *Geochim. Cosmochim. Acta* **46**, 637–649.

Kröner, A., Compston, W., William, I.S., 1989. Growth of early Archean crust in the Ancient Gneiss Complex of Swaziland as revealed by single zircon dating. *Tectonophysics* **161**, 271–298.

Kröner, A., Hegner, E., Wendt, J.I., Byerly, G.R., 1996. The oldest part of the Barberton granitoid-greenstone terrain, South Africa: evidence for crust formation between 3.5 and 3.7 Ga. *Precambrian Res.* **78**, 105–124.

Layer, P.W., Kröner, A., York, D., 1992. Pre-3000 Ma thermal history of the Archean Kaap Valley pluton, South Africa. *Geology* **20**, 717–720.

Loferski, P.J., Ayuso, R.A., 1995. Petrography and mineral chemistry of the composite Deboullie pluton, northern Maine, U.S.A.: implications for the genesis of Cu–Mo mineralization. *Chem. Geol.* **123**, 89–105.

Lopez Martinez, M., York, D., Hanes, J.A., 1992. A $^{40}Ar/^{39}Ar$ geochronological study of komatiites and komatiitic basalts from the Lower Onverwacht Volcanics: Barberton Mountain Land, South Africa. *Precambrian Res.* **57**, 91–119.

Lowe, D.R., 1999. Geologic evolution of the Barberton Greenstone Belt and vicinity. In: Lowe, D.R., Byerly, G.R. (Eds.), Geologic evolution of the Barberton Greenstone Belt, South Africa, v. Special Paper 329: Boulder, Geol. Soc. Amer., pp. 287–312.

Lowe, D.R., Byerly, G.R., 1999. Geologic evolution of the Barberton Greenstone Belt, South Africa, v. Special Paper 329: Boulder, CO, Geol. Soc. Amer.

Lucassen, F., Becchio, R., 2003. Timing of high-grade metamorphism: early Paleozoic U–Pb formation ages of titanite indicate long-standing high-T conditions at the western margin of Gondwana (Argetina, 26–29°). *J. Met. Geol.* **21**.

Ludwig, K.R., 1980. Calculation of uncertainties of U–Pb isotope data. *Earth Planet. Sci. Lett.* **46**, 212–220.

Ludwig, K.R., 1998. On the treatment of concordant uranium-lead ages. *Geochim. Cosmochim. Acta* **62**, 665–676.

Mattinson, J.M., 1994. Real and apparent concordance and discordance in the U–Pb systematics of zircons: limitations of "high-precision" U/Pb and Pb/Pb ages. *Eos* **75**, 691.

Mattinson, J.M., 2000. Revising the "gold standard"—the uranium decay constants of Jaffey et al., 1971. Eos Trans. AGU, Spring Meet. Suppl., Abstract V61A-02.

Mattinson, J.M., 2003. CA (chemical abrasion)-TIMS: high-resolution U–Pb zircon geochronology combining high-temperature annealing of radiation damage and multi-step partial dissolution analysis. Eos Trans. AGU, Fall Meet. Suppl., Abstract V22E-06.

Mattinson, J.M., 2005. Zircon U–Pb chemical-abrasion ("CA-TIMS") method: combined annealing and multi-step dissolution analysis for improved precision and accuracy of zircon ages. *Chem. Geol.* **220**, 47–56.

McDougall, I., Harrison, T.M., 1999. *Geochronology and Thermochronology by the $^{40}Ar/^{39}Ar$ method*. Oxford University Press, New York, NY.

Meurer, W.P., Boudreau, A.E., 1996. An evaluation of models of apatite compositional variability using apatite from the Middle Banded series of the Stillwater Complex, Montana. *Contrib. Miner. Petrol.* **125**, 225–236.

Mezger, K., Cosca, M.A., 1999. The thermal history of the Eastern Ghats Belt (India) as revealed by U–Pb and $^{40}Ar/^{39}Ar$ dating of metamorphic and magmatic minerals: implications for the SWEAT correlation. *Precambrian Res.* **1999**, 251–271.

Mezger, K., Hanson, G.N., Bohlen, S.R., 1989. High-precision U–Pb ages of metamorphic rutile: application to the cooling history of high-grade terranes. *Earth Planet. Sci. Lett.* **96**, 106–118.

Min, K., Mundil, R., Renne, P.R., Ludwig, K.R., 2000. A test for systematic errors in $^{40}Ar/^{39}Ar$ geochronology through comparison with U–Pb analysis of a 1.1 Ga rhyolite. *Geochim. Cosmochim. Acta* **64**, 73–98.

Mulch, A., Cosca, M.A., Handy, M.R., 2002. *In-situ* UV-laser $^{40}Ar/^{39}Ar$ geochronology of a micaceous mylonite; an example of defect-enhanced argon loss. *Contrib. Miner. Petrol.* **142**, 738–752.

Pan, Y., Fleet, M.E., 1996. Rare earth mobility during prograde granulite facies metamorphism: significance of flourine. *Contrib. Miner. Petrol.* **123**, 251–262.

Pan, Y., Fleet, M.E., 2002. Compositions of the Apatite-Group minerals: substitution mechanisms and controlling factors. In: Kohn, M.J., Rakovan, J., Hughes, J.M. (Eds.), *Phosphates: Geochemical, Geobiological, and Materials Importance, v. Reviews in Mineralogy and Geochemistry 48*. Mineralogical Society of America, Washington, DC, pp. 13–49.

Pidgeon, R.T., Bosch, D., Bruguier, O., 1996. Inherited zircon and titanite U–Pb systems in an Archean syenite from southwestern Australia: implications for U–Pb stability of titanite. *Earth Planet. Sci. Lett.* **141**, 187–198.

Rakovan, J., McDaniel, D.K., Reeder, R.J., 1997. Use of surface-controlled REE sectoral zoning in apatite from Llallagua, Bolivia, to determine a single-crystal Sm–Nd age. *Earth Planet. Sci. Lett.* **146**, 329–336.

Rakovan, J., Reeder, R.J., 1994. Differential incorporation of trace-elements and dissymmetrization in apatite—the role of surface-structure during growth. *Am. Mineral.* **79**, 892–903.

Reiners, P.W., Ehlers, T.A. (Eds.), 2005. *Low-Temperature Thermochrology: Techniques, Interpretations, and Applications: Reviews in Mineralogy and Geochemistry*, v. 58. The Mineralogy Society of America, Chantilly, VA.

Renne, P.R., Karner, D.B., Ludwig, K.R., 1998. Absolute ages aren't exactly. *Science* **282**, 1840–1841.

Royden, L.H., 1993. The steady-state thermal structure of eroding orogenic belts and accretionary prisms. *J. Geophys. Res.* **98**, 4487–4507.

Sano, Y., Terada, K., Hidaka, H., Yokoyama, K., Nutman, A.P., 1999. Paleoproterozoic thermal events recorded in the ~4.0 Ga Acasta gneiss, Canada: evidence from SHRIMP U–Pb dating of apatite and zircon. *Geochim. Cosmochim. Acta* **63**, 899–905.

Schmitz, M.D., Bowring, S.A., 2001. U-Pb zircon and titanite sytematics of the Fish Canyon Tuff: an assessment of high-precision U–Pb geochronology and its application to young volcanic rocks. *Geochim. Cosmochim. Acta* **65**, 2571–2587.

Schmitz, M.D., Bowring, S.A., 2003. constraints on the thermal evolution of continental lithosphere from U–Pb accessory mineral thermochronometry of lower crustal xenoliths, southern Africa. *Contrib. Miner. Petrol.* **144**, 592–618.

Schoene, B., Bowring, S.A., 2004. Rates and mechanisms of magma emplacement in the Usutu intrusive suite: implications for ca. 3.2 Ga assembly of the Kaapvaal craton. *G.S.A. abstracts with programs* **36**, 46.

Schoene, B., Bowring, S.A., 2006. U–Pb systematics of the McClure Mountain syenite: thermochronological constraints on the age of the $^{40}Ar/^{39}Ar$ standard MMhb. *Contrib. Miner. Petrol.* **151**, 615–630.

Schoene, B., Crowley, J.L., Condon, D.C., Schmitz, M.D., Bowring, S.A., 2006. Reassessing the uranium decay constants for geochronology using ID-TIMS U–Pb data. *Geochim. Cosmochim. Acta* **70**, 426–445.

Smith, M.P., Yardley, W.D., 1999. Fluid evolution during metamoprhism of the Otago Schist, New Zealand: (II) influence of detrital apatite on fluid salinity. *J. Metamorphic Geol.* **17**, 187–193.

Spear, F.S., 1993. *Metamorphic Phase Equilibria and Pressure–Temperature–Time Paths: MSA monograph*. The Mineralogical Society of America, Washington, DC, 799 p.

Spear, F.S., Pyle, J.M., 2002. Apatite, monazite, and xenotime in metamorphic rocks. In: Kohn, M.J., Rakovan, J., Hughes, J.M. (Eds.), *Phosphates: Geochemical, Geobiological, and Materials Importance: Reviews in Mineralogy and Geochemistry*, vol. 48. The Mineralogical Society of America, Washington, DC.

Stacey, J.C., Kramers, J.D., 1975. Approximation of terrestrial lead isotope evolution by a two-stage model. *Earth Planet. Sci. Lett.* **26**, 207–221.

Stevens, G., Droop, G.T.R., Armstrong, R.A., Anhaeusser, C.R., 2002. Amphibolite facies metamorphism in the Schapenburg schist belt: a record of the mid-crustal response to ~3.23 Ga terrane accretion in the Barberton greenstone belt. *S. Afr. J. Geol.* **105**, 271–284.

Turcotte, D.L., Schubert, G., 1982. *Geodynamics*. John Wiley, New York, 450 p.

Verts, L.A., Chamberlain, K.R., Frost, C.D., 1996. U–Pb sphene dating of metamorphism: the importance of sphene growth in the contact aureole of the Red Mountain pluton, Laramie Mountains, Wyoming. *Contrib. Miner. Petrol.* **125**, 186–199.

Viljoen, M.J., Viljoen, R.P., 1969. An introduction to the geology of the Barberton, granite–greenstone terrain. *Geol. Soc. S. Afr., Spec. Publ.* **9**, 1–20.

Wartho, J.-A., 1995. Apparent argon diffusive loss $^{40}Ar/^{39}Ar$ age spectra in amphiboles. *Earth Planet. Sci. Lett.* **134**, 393–407.

Watson, E.B., Harrison, T.M., 1984. Accessory minerals and the geochemical evolution of crustal magmatic systems: a summary and prospectus of experimental approaches. *Phys. Earth Planet. Int.* **35**, 19–30.

Watson, E.B., Harrison, T.M., Ryerson, F.J., 1985. Diffusion of Sm, Sr, and Pb in fluorapatite. *Geochim. Cosmochim. Acta* **49**, 1813–1823.

Waychunas, G.A., 2002. Apatite Luminescence. In: Kohn, M.J., Rakovan, J., Hughes, J.M. (Eds.), *Phosphates—Geochemical, geobiological, and materials importance*, v. 48. The Mineralogical Society of America, Washington, DC, pp. 701–742.

Westraat, J.D., Kisters, A.F.M., Poujol, M., Stevens, G., 2005. Transcurrent shearing, granite sheeting and the incremental construction of the tabular 3.1 Ga Mpuluzi batholith, Barberton granite–greenstone terrane, South Africa. *J. Geol. Soc. Lond.* **162**, 373–388.

Willmore, C.C., Boudreau, A.E., Kruger, F.J., 2000. The halogen geochemistry of the Bushveld Complex, Republic of South Africa: implications for chalcophile element distribution in the lower and critical zones. *J. Petrol.* **41**, 1517–1539.

Wilson, A.C., 1982. *1:250,000 Geological map of Swaziland*. Geological Survey Mines Department.

Wright, N., Layer, P.W., York, D., 1991. New insights into thermal history from single grain $^{40}Ar/^{39}Ar$ analysis of biotite. *Earth Planet. Sci. Lett.* **104**, 70–79.

Xie, X., Byerly, G.R., Ferrell, R.E., 1997. IIb trioctehedral chlorite from the Barberton greenstone belt; crystal structure and rock composition constraints with implications to geothermometry. *Contrib. Miner. Petrol.* **126**, 275–291.

Yardley, B.W.D., 1985. Apatite composition and fugacities of HF and FCl in metamorphic fluids. *Mineral. Mag.* **49**, 77–79.

Zhu, C., Sverjensky, D.A., 1991. Partitioning of F–Cl–OH between minerals and hydrothermal fluids. *Geochim. Cosmochim. Acta* **55**, 1837–1858.